



Chem Soc Rev

Nanoconfinement and Mass Transport in Metal-Organic Frameworks

Journal:	<i>Chemical Society Reviews</i>
Manuscript ID	CS-REV-06-2021-000558.R1
Article Type:	Review Article
Date Submitted by the Author:	07-Aug-2021
Complete List of Authors:	<p>Sharp, Conor; US Naval Research Laboratory, Electronic Science and Technology Division; Virginia Tech, Chemistry</p> <p>Bukowski, Brandon; Northwestern University, Department of Chemical & Biological Engineering</p> <p>Li, Hongyu; Stony Brook University, Department of Materials Science and Chemical Engineering</p> <p>Johnson, Eric; Virginia Tech, Department of Chemistry (MC 0212)</p> <p>Ilic, Stefan; Virginia Tech, Department of Chemistry (MC 0212)</p> <p>Morris, Amanda; Virginia Tech, Chemistry</p> <p>Gersappe, Dilip; Stony Brook University, Department of Materials Science and Chemical Engineering</p> <p>Snurr, Randall; Northwestern University, Department of Chemical & Biological Engineering</p> <p>Morris, John; Virginia Tech, Department of Chemistry (MC 0212)</p>

SCHOLARONE™
Manuscripts

Review Article

Nanoconfinement and Mass Transport in Metal-Organic Frameworks

Received 00th January 20xx,
Accepted 00th January 20xx

Conor H. Sharp,^a Brandon C. Bukowski,^b Hongyu Li,^c Eric M. Johnson,^d Stefan Ilic,^d Amanda J. Morris,^d Dilip Gersappe,^c Randall Q. Snurr,^b and John R. Morris^d

DOI: 10.1039/x0xx00000x

The ubiquity of metal-organic frameworks in recent scientific literature underscore their highly versatile nature. MOFs have been developed for use in wide array of applications, including: sensors, catalysis, separations, drug delivery, and electrochemical processes. Often overlooked in the discussion of MOF-based materials is the mass transport of guest molecules within the pores and channels. Given the wide distribution of pore sizes, linker functionalization, and crystal sizes, molecular diffusion within MOFs can be highly dependent on the MOF-guest system. In this review, we discuss the major factors that govern the mass transport of molecules through MOFs at both the intracrystalline and intercrystalline scale; provide an overview of the experimental and computational methods used to measure guest diffusivity within MOFs; and highlight the relevance of mass transfer in the applications of MOFs in electrochemical systems, separations, and heterogeneous catalysis.

1. Introduction

Over the last two decades, metal-organic frameworks (MOFs) have emerged as a set of materials that demonstrate exceptional promise in a wide variety of applications. MOFs are comprised of metal-oxo or metal-based inorganic clusters and organic linkers/secondary building units (SBUs) that assemble into extended porous 2-dimensional and 3-dimensional networks.¹ The pore sizes of MOFs can vary significantly based on linker and node, typically ranging from the microporous (<2 nm) to mesoporous (2 to 100 nm) regimes. Unlike other porous materials such as activated carbons, the porosity of MOFs is typically well-defined and uniform throughout the crystal structure. Due to the wide variety of oxide SBUs and bridging ligands, thousands of different MOF structures have been described, with more synthesized each year.² The synthetic control over MOF pore structure and chemical functionality has made MOFs highly promising materials in a wide variety of fields, including gas storage, catalysis, separations, electrochemical applications, and many more.³ Relevant to virtually every application of MOFs is the diffusion of guest molecules.

Molecular diffusion, characterized by the diffusion coefficient, is a fundamental measure of the ability of molecules to pass through

a specific medium.⁴ Diffusion can be characterized by a number of different diffusion coefficients or diffusivities. Two of the most common are the transport diffusivity (also known as the Fickian diffusivity) and the self-diffusivity. The transport diffusivity characterizes mass transfer due to a concentration or chemical potential gradient, whereas the self-diffusivity characterizes the random Brownian motion of a system at equilibrium with no chemical potential gradient.⁵ In mesoporous media, the mechanism of diffusion is typically characterized by the Knudsen number, which is defined as the ratio of the mean free path length of the diffusing molecule to the pore size of the medium.⁶ In mesoporous media such as some MOFs, the mean free path is affected by two factors: the collisions between diffusing molecules (gas-gas/fluid-fluid collisions) and the collisions between molecules and structures (gas(fluid)-wall collisions). Collisions between the gas and the wall affect the diffusion in two possible ways: one, by simply affecting the mean free path, and two, by possible adsorption/desorption events. When adsorption and desorption events limit molecular transport, the process can be described as activated diffusion. In the absence of rate-limiting molecule-support interactions, diffusion is referred to as non-activated. For activated diffusion, the diffusion constant, D , has been empirically shown to follow an Arrhenius-type dependence where $D = D_0 \exp(-E_A/kT)$, with E_A representing the activation energy, k the Boltzmann constant, T the temperature, and D_0 the pre-exponential factor. Studies have shown that this activation energy can be related to several factors such as hydrogen bonding, desorption and re-adsorption process, and the tortuosity of the structure.⁷

In MOFs, the nanoporous structure results in reduced diffusion coefficients that can be several orders of magnitude lower than diffusion through air.⁸ Hindered diffusion of molecules within

^a National Research Council Associateship Program and Electronic Science and Technology Division, U.S. Naval Research Laboratory, Washington, DC 20375, United States.

^b Department of Chemical and Biological Engineering, Northwestern University, Evanston, Illinois 60208, United States.

^c Department of Materials Science and Chemical Engineering, Stony Brook University, Stony Brook, New York 11794, United States.

^d Department of Chemistry, Virginia Tech, Blacksburg, Virginia 24061, United States.

nanoporous materials, which significantly decreases the diffusion coefficient, is an important effect of nanoconfinement.⁹ Previous reviews that have discussed guest diffusion through MOFs have focused either more broadly on diffusion through porous crystalline materials,¹⁰⁻¹² or discuss diffusion as it specifically relates to one specific application of MOFs, such as *in operando* methods for analyzing diffusion during MOF-based catalysis.¹³ In the following review, we summarize the key factors that govern the mass transport of molecules through MOFs, provide a background on the experimental and computational methods used to effectively measure/calculate diffusivity of gases and liquids through MOFs, and discuss the relevance of mass transfer in the applications of separations, electrochemical processes, and heterogeneous catalysis.

2. Factors that Influence Diffusion in MOFs

Molecular transport into, out of, and through MOF materials is governed by a complex dynamic of structural and chemical factors that are often interdependent. These factors affect diffusion at the atomic scale in ways that, due to the tremendous internal surface area associated with MOFs, often lead to large effects on bulk transport as measured in macroscopic systems. In this section, we discuss how the intrinsic and dynamic structures of a MOF affect the ability of guest molecules to enter and diffuse through its pores, how defects can either increase or hinder guest diffusion, the effect that intercrystalline diffusion can have on the physically observed mass transport, and how chemical interactions between diffusing molecules and either the MOF or other diffusants can restrict transport.

2.1 Pore Size Effects

The size of the MOF pores has critical implications for guest diffusion. In MOFs,¹⁴ narrow channels lead to increased guest-host interactions, and narrow window regions can result in high activation barriers for diffusion. For example, changes to the size of the MOF pore aperture as small as 0.2 Å resulted in pronounced changes in the diffusivities of propane and propylene in several zeolitic imidazolate framework (ZIF) MOFs.¹⁵ A number of recent studies have systematically examined how MOF pore and aperture size affect diffusion by employing isorecticular MOFs, systematically synthesized by modulating the organic linker length.¹⁶ Forse et al. measured the self-diffusion of CO₂ within two isorecticular MOFs, Zn₂(dobdc) and Zn₂(dobpdc).¹⁷ The longer dobpdc (4,4'-dioxidobiphenyl-3,3'-dicarboxylate) linkers of Zn₂(dobpdc) expand the diameter of the hexagonal channels from 15 Å to 22 Å, as compared to Zn₂(dobdc) (**Fig. 1**).¹⁷ For diffusion along the hexagonal channels of each MOF, CO₂ was shown to diffuse at least a factor of 4 faster in the larger-pore Zn₂(dobpdc). The increase in diffusivity with increasing pore size was attributed to a combination of the decrease in the energetic barrier to diffusion through the center of the channel (i.e. reduced dispersion interactions) and a decrease in adsorption strength at the Zn binding sites. Changes in linker functionality can also have an effect on the diameter of the pore aperture, and subsequently, guest diffusion. The self-diffusion of a series of polar and non-polar solvent molecules were measured in

two isorecticular Zn-based MOFs, MOF-5 (Zn₄O(BDC)₃) and IRMOF-3.¹⁸ For every solvent studied, the molecules diffused more slowly through IRMOF-3. It was hypothesized that the presence of the amine groups on the linker of IRMOF-3 minimized the size of the pore aperture, restricting transport into the MOF.

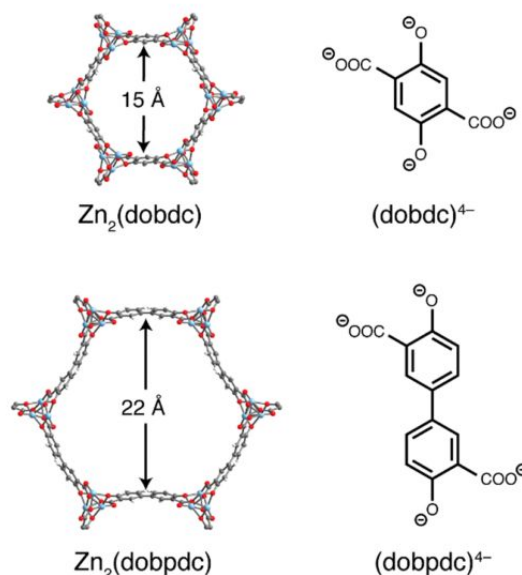


Fig. 1 Single pore of Zn₂(dobdc) and Zn₂(dobpdc) alongside illustrations of their respective ligands. Pale blue, grey, red, and white spheres represent Zn, C, O, and H atoms, respectively. Figure adapted with permission from A. C. Forse, K. A. Colwell, M. I. Gonzalez, S. Benders, R. M. Torres-Gavosto, B. Blümich, J. A. Reimer, J. R. Long, A. C. Forse, K. A. Colwell, M. I. Gonzalez, S. Benders, R. M. Torres-Gavosto, B. Blümich, J. A. Reimer and J. R. Long, *Chemistry of Materials*, 2020, **32**, 3570-3576. Copyright 2021 American Chemical Society.

2.2 Pore Topology

The topology of a given MOF governs the spatial positioning and connectivity of nodes and linkers that define the shape and distribution of pores. Not only can topology affect the mass transport kinetics, but it can also affect the mechanism by which guest molecules move through the pores. There have been very few systematic studies of the role of topology on diffusion in MOFs to date. In one of the few examples, Bukowski and Snurr performed molecular dynamics simulations for MOFs from over 20 different topologies that share similar linkers and have Zr₆ nodes and examined the role of connectivity and topology on alkane diffusion.¹⁹ They found that Zr MOFs with higher node connectivity have slower average alkane diffusion, but the linker connectivity had a minimal effect on the diffusivity. Diffusion coefficients did not correlate well with pore size descriptors, which further suggested that topology-focused descriptors could be developed to identify MOFs with rapid adsorbate diffusion using high-throughput simulations. This may be an interesting area for future work.

2.3 Linker Dynamics and Framework Flexibility

While nominal MOF pore and aperture diameters can be determined from crystallographic data, the size and structure of MOF pores can

Review Article

vary due to their linker dynamics, which can be a function of temperature and chemical environment. Molecular dynamics simulations of CH₄ self-diffusion in UiO-66 highlight the importance of the effect of lattice dynamics on diffusion.²⁰ The CH₄ self-diffusion coefficients simulated incorporating MOF framework flexibility had better agreement with experimental values than diffusion coefficients simulated while holding the framework rigid. The incorporation of flexibility in the force field also allowed for a better understanding of the intercage guest hopping between the tetrahedral and octahedral cages of UiO-66, which is significantly influenced by the rotation of the 1,4-benzenedicarboxylate (BDC) linkers.^{20, 21} In general, the use of force fields that account for framework flexibility is required when the MOF undergoes structural transformations or when the size of the guest molecule is similar to the pore size of the MOF.²² Devautour-Vinot et al. probed the structural dynamics of several UiO-66 MOFs with functionalized BDC linkers and observed that the activation barrier to linker rotation was as high as 12.4 kcal/mol due to intraframework interactions.²³ For ZIF-8, the rotations of the 2-methylimidazolate linkers upon exposure to high gas pressures (>1.47 GPa) result in an increase in the pore diameter from 3.0 Å to 3.6 Å,²⁴ which could significantly affect diffusion. Gonzalez-Nelson et al. provide a detailed review of the effects of rotational dynamics on guest adsorption and diffusion in MOFs.²⁵

In addition to the effect of linker rotation on MOF pore size and accessibility, certain “flexible” MOFs can undergo structural rearrangements in the presence of external stimuli, affecting their pore size and transport properties. Agrawal and Sholl found that when modeling gas adsorption and diffusion, framework flexibility was most important when investigating the uptake of molecules with kinetic diameters that are close to those of the MOF pores.²⁶ For the flexible MOF MIL-53(Cr), which transitions from a large-pore (LP) phase to a narrow-pore (NP) phase (Fig. 2) at low CO₂ loadings and then to LP at high CO₂ loadings, CO₂ diffuses approximately two orders of magnitude faster through the LP form.²⁷ While the CO₂ diffusion proceeds through a similar site-hopping mechanism through both phases of MOF, the activation energy of diffusion was lower in the LP form of MIL-53(Cr) due to a decrease in pore-wall interactions. STAM-1, a MOF containing both hydrophobic and hydrophilic pores, undergoes a “gate-opening” transition upon exposure to polar molecules, increasing the diameter of the hydrophobic pore from 5.4 Å to 6.3 Å, resulting in an increase in the diffusivity of adsorbed methanol.²⁸ In addition to chemically-induced phase changes, Knebel et al. demonstrated that the application of an external electric field on ZIF-8 can be used to induce a phase change and tune the separation efficiency for light alkanes.²⁹ A 500 V/mm electric field was applied perpendicular to a 20 μm-thick MOF layer, inducing a phase change from the standard cubic phase to a monoclinic phase. This resulted in a stiffening of the lattice, restricting linker rotations and reducing guest diffusion.

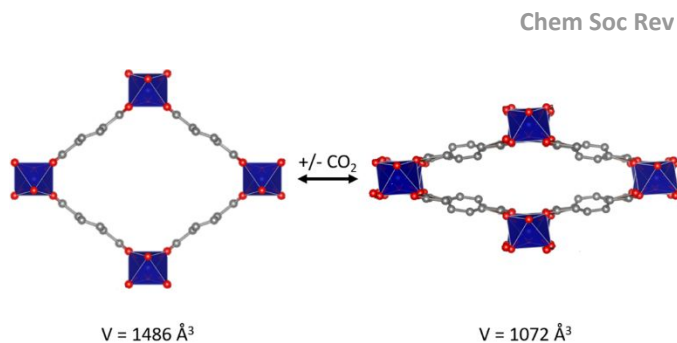


Fig. 2 Structural transitions between large-pore (left) and narrow-pore (right) phases of MIL-53(Cr) upon CO₂ adsorption.

2.4 Defects and Surface Barriers

Point defects in MOFs, introduced via synthesis or exposure to humidity and other reactive conditions, can affect the energy barriers and tortuosity of guest diffusion within MOFs. In MOFs, defects typically exist as either missing linkers, dangling linkers, missing inorganic nodes, or nodes capped by modulators used in synthesis. Han, Verploegh, and Sholl assessed the role of defects on mass transport in ZIF-8 using molecular simulations and found that an increase in linker vacancies and dangling linker defects resulted in faster hopping rates for several light alkanes.³⁰ However, if the missing linker molecules remained confined within the ZIF-8, there was a significant decrease in diffusivity due to pore-blocking effects. When located near the external surface of a crystal or film, these defects can also act as surface barriers.

Heinke et al. demonstrated that while pristine films of HKUST-1 showed no evidence of surface barriers, once films were exposed to either water vapor or an ambient atmosphere, the formation of defects led to reduced surface permeability and decreased uptake of cyclohexane.³¹ They speculated that the defects resulted in pore blockage and an increase in strong binding sites for cyclohexane, both of which result in a decrease in the diffusivity. Recently, Müller et al. demonstrated that surface defects in HKUST-1 films caused by water vapor exposure could be removed by exposing the MOF to an ethanolic solution.³² Quartz crystal microbalance measurements showed that the removal of these defects result in a restoration of the uptake and permeability rates of the MOF films to their pre-defected behaviors.

Some MOFs are intentionally synthesized with defects to increase pore size, increase the number of active sites, or tune the chemical functionality of the MOF. Defect-engineering MOFs can create mesoporous domains that facilitate faster guest diffusion.³³ Yuan et al. synthesized PCN-160 with a fraction of 4-carboxybenzylidene-4-aminobenzoate (CBAB) linkers.³⁴ Upon the introduction of acetic acid, the CBAB linkers were split into monotopic 4-aminobenzoic acid and 4-formylbenzoic acid linkers and then removed from the MOF by acid etching (Fig. 3). This process created a hierarchical pore structure through the introduction of missing linkers and missing nodes defects, which enabled the uptake of large guest molecules. A further discussion of defect-engineering and MOF diffusion is provided by Xiang et al.³⁵

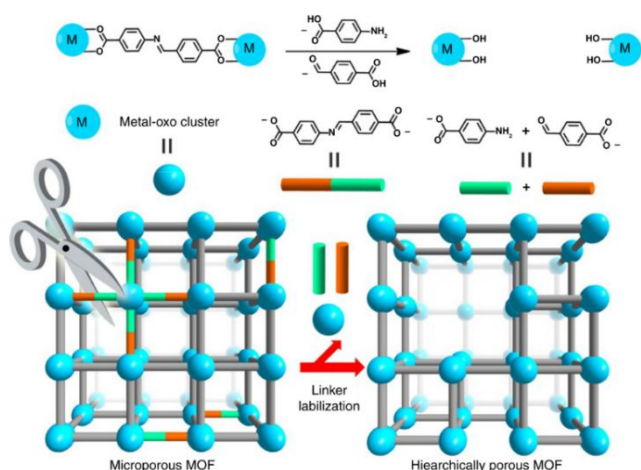


Fig. 3 Labilization of CBAB linker to create hierarchically porous MOF. Figure adapted with permission from S. Yuan, L. Zou, J.-S. Qin, J. Li, L. Huang, L. Feng, X. Wang, M. Bosch, A. Alsalmeh, T. Cagin and H.-C. Zhou, *Nature Communications*, 2017, **8**, 15356.

Not all surface barriers are the result of defects; intentional surface barriers can be synthesized onto MOFs to act as capping agents to improve separation efficiency, hindering diffusion and desorption of guest molecules within a given MOF. Under UV excitation, β -cyclodextrin (β -CD) strongly adsorbs to the surface of UiO-68 with azobenzene-functionalized linkers (UiO-68-azo), acting as a capping ligand that reduces the effective pore aperture size.³⁶ The β -CD surface barrier reduced the permeability of CO_2 more significantly than H_2 , resulting in an improved separation selectivity of H_2/CO_2 . Homan et al. functionalized the surface of MOF-5 with capping groups and found that biphenyl- and triphenylacetic acid capping ligands effectively prevented the diffusion and desorption of crystal violet from the MOF pores.³⁷

Whether through incomplete synthesis, intentional design, or reactive chemical environments, the presence of defects within MOFs can greatly affect guest diffusion. Missing linker defects may increase effective pore sizes and facilitate faster intercage diffusion rates, but may also result in stronger adsorption sites for guest molecules on the inorganic SBUs. Defect-induced or synthesized surface barriers may have little effect on the diffusion of guest molecules within the interior of the MOF crystals, but may limit the mass transfer between adjacent MOF crystals by decreasing the surface permeability.

2.5 Effects of intercrystalline pores and crystal size

While most factors discussed above pertain to the diffusion of molecules through the interior pores of a given MOF crystal (intracrystalline diffusion), it is often necessary to consider transport between crystals (intercrystalline diffusion) to gain a comprehensive view of mass transport at the macroscopic scale. For MOF powders and pelletized samples, grain boundary diffusion and intercrystalline diffusion significantly contribute to the overall mass transport. It is therefore important to understand how these factors affect overall diffusion in MOF materials.

In pelletized MOF-5 samples, Xu et al. found that increasing pellet density correlates with a decrease in H_2 diffusivity.³⁸ The densities of the measured MOF-5 samples were found to be lower than the theoretical density for a single MOF-5 crystal,³⁹ suggesting that void spaces between crystallites exist in the pelletized powder samples and create small macropore regions where intercrystalline diffusion occurs faster than the intracrystalline diffusion. Intercrystalline diffusion can sometimes be the rate-limiting process for diffusion in pelletized samples or through a bed of MOF crystals. Krishnamurthy studied the diffusion of CO_2 in pelletized beads of CPO-27-Ni and determined that diffusion through the macropores was the rate-limiting step. Similar results have been reported for CO_2 and water diffusion in HKUST-1 and Ni/DOBDC.^{40, 41} As described below, determining the effect that intercrystalline and intracrystalline diffusion have on overall mass transport requires the use of specialized experimental techniques.

Zhang et al. employed a combination of experimental and computational techniques to study the effect of crystallite size on adsorbate-induced structural transitions for nitrogen (N_2) adsorption within ZIF-8. Interestingly, the crystal size of ZIF-8 affected the propensity of the MOF to undergo structural transitions. Specifically, the gate-opening mechanism for the MOF, which results in an increase in mass transport, was found to occur at lower N_2 pressures for larger-sized crystals.⁴² In addition, Tanaka et al. studied the effect of crystal size on the transport of *n*-butanol through ZIF-8 and determined that a decrease in crystal size led to an increase in the effect that surface barriers had on diffusion measured through the sample.⁴³

2.6 Guest-MOF Interactions

The energetic interactions between guest molecules and the internal pore environments of MOFs have a significant impact on diffusion. For molecules that diffuse via a site-hopping mechanism, strong binding energies at adsorption sites result in high activation barriers for diffusion, reducing mass transport.⁴⁴ Hydroxyl groups found on the inorganic nodes of several MOFs can act as Brønsted-acid, hydrogen-bond donors where guest molecules can adsorb.^{45, 46} Wardzala et al. calculated the diffusivity of acetone through UiO-66 using molecular dynamics simulations and observed that hydrogen bonding between acetone and the $\mu_3\text{O}-\text{H}$ groups at the zirconium nodes resulted in up to an order of magnitude decrease in diffusivity compared to UiO-66 MOFs with the hydroxyls removed.⁴⁷ The confined nature of guest molecules within the pores and channels of a MOF, coupled with a tremendously high number of potential adsorption sites, render energetic contributions from dispersion interactions particularly significant for diffusivities relative to other, non-porous surfaces. Liu et al. performed molecular simulations of benzene diffusion through Mg-MOF-74 and determined that benzene-pore wall interactions were dominated by van der Waals interactions, which result in very low diffusivities.⁴⁸ A variety of experimental techniques exist to identify and quantify guest-MOF interactions, including single-crystal X-ray diffraction,⁴⁹⁻⁵² infrared spectroscopy,⁵³⁻⁵⁶ and temperature-programmed desorption.^{57, 58}

Guest-MOF interactions have also been shown to induce structural changes within flexible MOFs, which can be exploited for improved molecular transport and adsorption capacity. Zhao et al. observed that for the adsorption of CO₂ within ZIF-7 at low pressures, adsorption is limited within only one of the six-member-ring pores (pore B) (Fig. 4).⁵⁹ The other six-member-ring pore (pore A) has a pore aperture of 3 Å, which is too small for CO₂ (kinetic diameter = 3.3 Å) to pass through. However, at increased CO₂ pressures, hydrogen bond formation between adsorbed CO₂ and a benzimidazolate linker shared between pore A and pore B induces a linker rotation that enables CO₂ adsorption and diffusion into pore A.

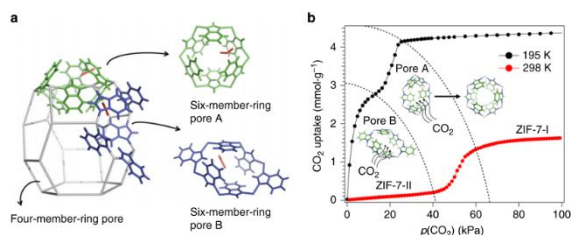


Fig. 4 ZIF-7 structure and CO₂ adsorption behavior. **a** The building unit, a sodalite cage, of ZIF-7 with two types of six-member-ring pores (A, B) and one type of four-member ring pores on its walls. **b** CO₂ adsorption isotherms of ZIF-7 at 195 and 298 K, $p(\text{CO}_2) = 1$ –100 kPa, illustrated by the structural behaviors of ZIF-7. Figure adapted with permission from Zhao, P., Fang, H., Sanghamitra, M., Li, A., Rudić, S., McPherson, I.J., Tang, C.C., Fairen-Jimenez, D., Tsang, S.C.E., Redfern, S.A.T, Nature Communications, 2019, **10**, 1.⁵⁹

2.7 Loading and Guest-Guest Interactions

In addition to the interactions between guest molecules and the pore walls and nodes of a MOF, the interactions between guest molecules themselves (either in single-component or multi-component mixtures) can have a significant effect on their diffusivities. The loading dependence of self-diffusion coefficients can vary depending on the guest molecule and MOF, but typically exhibit a monotonic decrease with increasing guest concentration.²¹ At high guest concentrations, increased guest-guest collisions and a decrease in free pore volume causes self-diffusivities to decrease. The loading can also have a significant effect on diffusion coefficients in flexible MOFs that undergo “gate-opening” and other structural rearrangements.⁶⁰ For example, Salles et al. observed that, for water diffusion through the flexible MOF MIL-53(Cr), the self-diffusion coefficients decreased with increasing water loading from 0 to 8 water molecules per unit cell for both the narrow-pore and large-pore phases.⁶¹ This was attributed to a combination of a decrease in free pore volume as well as the attractive interactions with other confined water molecules. The calculated self-diffusivity of water through UiO-66 increased with loadings up to 100 H₂O molecules per unit cell, then decreased at higher concentrations due to hydrogen bonding between water molecules accompanied by a pore volume decrease.⁶² Importantly, we note that while self-diffusivities often decrease at high guest concentrations, transport diffusivities typically increase with loading due to the increasing thermodynamic factor,^{63–65} which is discussed in section 3.2.2.

Multicomponent mixture diffusion, or the transport of multiple guest species simultaneously, has not been extensively studied in MOFs, but is of high importance for understanding transport *in operando* for separations, catalysis, and other practical applications of MOFs. In some instances, the presence of polar or electronegative guest molecules can hinder the diffusion of non-polar diffusants. For example, CO₂ diffuses more slowly through Mg-MOF-74 when water is the predominant guest species, because adsorbed water forms clusters that act as binding sites for the CO₂.⁶⁶ Tan et al. also observed that for the diffusion of CO₂ through Ni-MOF-74, the presence of ammonia adsorbed at coordinatively unsaturated Ni sites increased the energetic barrier for CO₂ transport by a factor of 7, due to the presence of hydrogen-bonding interactions between the CO₂ and adsorbed ammonia.⁶⁷ In some cases, the presence of other guest molecules has been shown to have a minor effect or even improve guest diffusivity. The presence of long-chain alkanes has a minimal effect on the diffusion of methane through MOFs PCN-14, NU-1225, NU-1100, and DUT-49,⁶⁸ but hydrogen was found to cause an increase in methane diffusivity through ZIF-68 and ZIF-70 due to momentum transfer.⁶⁹

3. Techniques for Measuring and Calculating Guest Diffusion in MOFs

Developing a comprehensive understanding of the kinetics, energetics, and mechanisms of mass transport within MOFs poses a scientific challenge that demands the implementation of precision experimental and computational techniques capable of discerning small differences between similar systems. Many of the techniques utilized to measure guest diffusion with MOFs have also been implemented to investigate the transport of molecules in zeolites and other porous materials.^{70–78} A current issue facing the discussion of mass transport in MOFs is the large variation of reported diffusion coefficients in the literature for similar MOF-guest systems.⁷⁹ These differences are often attributed to a combination of factors that include varying experimental methods that measure diffusion at different length- and time-scales; inconsistencies in nominally identical MOF samples due to subtle differences in syntheses; and varying sample form (powder, single-crystal, film, pellet, etc.), which can introduce additional mass transfer effects. Computational methods can also yield different predictions for diffusion coefficients on nominally identical MOFs due to differing force fields. Robust studies of guest diffusion through MOFs therefore require an ensemble of complementary techniques, often leveraging both computational and experimental approaches.

3.1 Experimental Methods

An array of experimental techniques exists for quantifying mass transport in MOFs, and they can be classified into several overarching categories: gravimetric and mass balance techniques, spectroscopic techniques (both equilibrium and non-equilibrium), and microscopy. Diffusion coefficients are typically measured over a range of guest

concentrations and temperatures to determine how both factors affect molecular transport. The temperature dependence of the diffusivity can be evaluated by fitting the measured diffusion coefficients with an Arrhenius-like expression:

$$D(T) = D_0 e^{-\frac{\Delta E_{diff}}{RT}} \quad (1)$$

In Eq. 1, $D(T)$ is the diffusion coefficient at a given temperature, D_0 is the diffusion coefficient at infinite temperature, ΔE_{diff} is the activation energy of diffusion, and R is the gas constant. Assuming a site-hopping diffusion mechanism, the D_0 term can be used to further determine both hopping distance (a) and attempt frequency (ν_0).^{80, 81}

$$D_0 = \frac{1}{6} a^2 \nu_0 \quad (2)$$

Below, we introduce several common methods employed to measure guest diffusion in MOFs and highlight their strengths and limitations.

3.1.1 Gravimetric and Mass Balance Techniques In gravimetric approaches for studying transport within MOFs, the MOF samples (typically loose powders or pelletized MOF crystals) are placed on a balance that is sensitive to μg -level changes in mass (microbalance).^{11, 72} Upon gas exposure, the change in sample mass is attributed to gas adsorption and recorded as a function of time. Zhao et al. measured the transient adsorption for CO_2 within loose crystals of MOF-5 and fit the uptake curve with an equation used to describe diffusion within a sphere:⁸²

$$\frac{q_t}{q_e} \cong \frac{6}{r_c \sqrt{\pi}} \sqrt{Dt} \quad (3)$$

In Eq. 3, q_t is the mass loading at time t , q_e is mass loading at equilibrium, r_c is the radius of the crystal, and D is the intracrystalline diffusion coefficient. Note that Eq. 3 is an approximation that holds at short times.¹¹ Uptake kinetics can be similarly measured using the volumetric method, in which two cells, one containing a known pressure of dosing gas and another containing the MOF sample are connected by a closed valve.⁸³ After the valve is opened, the change in pressure is measured until the system equilibrates. At equilibrium, the measured mass loadings provide the adsorption isotherm and can be used to determine isosteric heats of adsorption if isotherms are obtained at several temperatures.⁸² Like several of the other techniques, the method requires fairly large crystals of uniform crystallite sizes for the accurate extraction of diffusion coefficients. Wang et al. recently reviewed best practices and discuss common pitfalls to avoid.⁷²

A quartz crystal microbalance (QCM), which measures the frequency of a piezoelectric quartz crystal, has been used to study the diffusion of both vapors and liquids in very thin MOF films deposited on the quartz crystal.⁸⁴ In QCM-based methods, an alternating current is applied to a quartz crystal that induces oscillations and generates a standing shear wave.⁸⁰ The frequency of this oscillation is perturbed upon guest adsorption and the mass

loading of adsorbed molecules is determined through the Sauerbrey equation⁸⁰:

$$\Delta f_n = -2n f_F^2 \frac{M_f}{C} \quad (4)$$

where Δf_n represents the change in frequency at the n th overtone order, f_F is the frequency of the fundamental standing wave, M_f is mass loading, and C is a constant that accounts for the velocity of sound and the density of the crystalline quartz. Heinke et al. employed QCM to measure the diffusion coefficients of cyclohexane within HKUST-1 films of varying film thickness to determine the extent to which surface barriers affect the overall uptake process.³¹ QCM requires the growth of uniform MOF films, and because films must remain thin enough for the Sauerbrey equation to remain valid, QCM is limited to measuring slow diffusivities on the order of $6 \times 10^{-19} \text{ m}^2 \text{ s}^{-1}$ to $6 \times 10^{-13} \text{ m}^2 \text{ s}^{-1}$.⁸⁴

The zero-length column (ZLC) technique has primarily been used to study adsorption kinetics in zeolites but has recently been used to study MOFs.^{40, 85} In ZLC, a thin layer of MOF crystals or pellets is exposed to an adsorbate under carrier gas flow conditions. The in-MOF concentration of the adsorbate is measured by tracking both flow rate and mass spectrometric signal. After the guest uptake has reached equilibrium, the gas flow is then switched to the carrier-gas only and the decrease in adsorbate concentration is recorded over time. Assuming that only one diffusion process acts as the rate-limiting diffusion process, the Fickian diffusion coefficient from spherical particles is determined by fitting the data to the following equation:⁸⁵

$$\frac{C_t}{C_0} = \sum_{n=1}^{\infty} \frac{2L e^{-\beta_n^2 \frac{D}{r^2} t}}{\beta_n^2 + (\gamma_z \beta_n^2 + 1 - L)^2 + \gamma_z \beta_n^2 + L - 1} \quad (5)$$

where C_t is the concentration at time t , C_0 is the concentration at equilibrium, L is the ratio of the diffusional time constant and convective desorption time, γ_z is the ratio of the hold up in the fluid phase to the accumulation in the solid phase, and β_n is determined from the equation

$$\beta_n \cot \beta_n + L - 1 + \gamma_z \beta_n^2 = 0 \quad (6)$$

Due to the minimal sample thickness in ZLC, the system can be assumed to be well-mixed and external mass transfer can be neglected.⁸⁵ For pelletized MOF samples, comparing ZLC concentration curves with varying flow rate can determine whether mass transfer is limited by diffusion within the MOF crystals (intracrystalline or micropore diffusion) or diffusion in void spaces between the crystals (macropore diffusion).⁸⁵

Concentration swing frequency response (CSFR) is another flow technique that has been used to measure the diffusion of both gases⁸⁶ and condensable vapors in MOFs.^{86, 87} In CSFR, the concentration of analyte gas/vapor undergoes a sinusoidal perturbation with a constant amplitude ($\Delta y_{i,in}$) and frequency (ω) while flow rate and pressure in the MOF sample bed are kept constant. The amplitude at the output of the sample bed ($\Delta y_{i,out}$) is measured via mass spectrometry. The amplitude ratio of $\Delta y_{i,out} / \Delta y_{i,in}$ is plotted as a function of ω and the data is then fit with diffusion

models describing micropore or macropore diffusion. The micropore diffusion model for CSFR is

$$\frac{\partial C}{\partial t} = \frac{D}{r^2} \frac{\partial}{\partial r} \left(r^2 \frac{\partial C}{\partial r} \right) \quad (7)$$

$$C = C_0(P, T) \text{ at } r = r_c \quad (8)$$

$$\frac{\partial C}{\partial t} = 0 \text{ at } r = 0 \quad (9)$$

where C is the adsorbed phase concentration, C_0 is the adsorbed phase concentration at equilibrium, r is the radial coordinate, r_c is the radius of the crystallites, D is the micropore diffusivity, and t is time.⁸⁷ Macropore diffusion is modeled by:⁸⁷

$$\frac{\partial C}{\partial t} = \frac{1}{\left(1 + \frac{\rho_p K}{\varepsilon_p}\right)} \frac{D}{r^2} \frac{\partial}{\partial r} \left(r^2 \frac{\partial C}{\partial r} \right) \quad (10)$$

where ρ_p is particle density, K is the local slope of the isotherm, and ε_p is the macroporosity. Additional modeling of the CSFR response curves has been used to account for surface barrier resistance.⁸⁸ Evaluation of the model fits at a range of feed pressures can help determine whether macropore or micropore diffusion is the rate-limiting step for the mass transfer. While CSFR has typically been used on MOF powders or pelletized samples, Tovar et al. used CSFR to measure the diffusivity of CO₂ within millimeter-scale single crystals of Cu-BTC.⁷⁹ CSFR has also been used to evaluate mixture diffusion in nanoporous materials,⁸⁸ but has yet to be employed for mixtures in MOFs.

3.1.2 Spectroscopic Methods Unlike gravimetric and mass balance methods, spectroscopic techniques provide molecular-level insight into the dynamics of guest molecules within the MOF pores, help identify diffusion mechanisms, and often measure diffusion at shorter length and time scales. The insights gained from spectroscopic methods can be used to further develop computational methods for investigating diffusion (vide infra). Spectroscopic methods can be characterized as either equilibrium or non-equilibrium techniques. Equilibrium techniques, such as NMR and incoherent quasi-elastic neutron scattering (QENS), measure the self-diffusion of molecules, while non-equilibrium techniques, such as coherent QENS and infrared (IR) spectroscopy, are used to determine transport diffusivity.

Quasi-elastic neutron scattering (QENS) is a powerful tool that yields quantitative information on the rotational, vibrational, and translational motions of guest molecules within MOFs.⁸⁹ QENS experiments require high intensity neutron sources, such as those found at large neutron accelerator facilities, of which only a few exist in the world.⁹⁰ In a QENS experiment, the broadening of the elastic neutron line is caused by small energy transfers (± 2 meV) between the incident neutrons and the atoms in the sample.⁹⁰ Due to the large incoherent scattering cross section of hydrogen, the scattering intensity in QENS is primarily attributed to the motions of hydrogen. Deuterated MOF samples are often used to minimize scattering attributed to the MOF framework. The contributions to the

incoherent scattering intensity due to the self-diffusion of guest molecules can be described by the Lorentzian function:^{90, 91}

$$S_{incoherent}^{trans}(Q, \omega) = \frac{1}{\pi} \frac{\Delta\omega(Q)}{\omega^2 + [\Delta\omega(Q)]^2} \quad (11)$$

In Eq. 11, $S_{incoherent}^{trans}$ is the incoherent translational scattering intensity, Q is the scattering vector, and $\hbar\omega$ is the neutron energy transfer. The half width at half maximum (HWHM) in the Fickian diffusion regime is described by $\Delta\omega(Q) = D_{self}Q^2$, where D_{self} is the self-diffusion coefficient. By plotting the HWHM as a function of Q^2 , it is possible to determine the self-diffusion coefficient. For deuterated- and non-hydrogen-containing guest molecules, coherent QENS can measure transport diffusion.⁹² The coherent scattering intensity can be described by the equation:

$$S_{coherent}^{trans}(Q, \omega) = \frac{S(Q)}{\pi} \frac{\Delta\omega(Q)}{\omega^2 + [\Delta\omega(Q)]^2} \quad (12)$$

where $S(Q)$ is a structure factor. To measure translational diffusion with QENS, the probed length scale ($\lambda = \frac{2\pi}{Q}$) must be greater than the length of the MOF cavities.⁹¹ At high Q values, QENS is used to extract mechanistic information about the diffusion process. The scattering intensity for random-jump diffusion can be described with a Lorentzian function with HWHM:⁸⁹

$$\Delta\omega(Q) = \frac{1}{\tau} \frac{\sin(Qd)}{Qd} \quad (13)$$

where τ is the residence time at a given site and d is the jump length. Given the short length-scale that is probed by incident neutrons, QENS can measure diffusion phenomena that are inaccessible by other techniques. Jobic used QENS to observe and quantify the first reported instance of single-file diffusion in a MOF, where guest molecules cannot pass one another while diffusing, for the transport of neopentane in MIL-47(V).⁹³

NMR was the first experimental technique used to examine self-diffusion within MOFs and has remained a valuable tool for measuring molecular transport within MOFs.⁹⁴ The most common NMR technique for studying diffusion is pulsed field gradient NMR (PFG NMR).^{11, 74, 75} In PFG NMR, MOF samples are typically exposed to known concentrations of a gas or vapor and sealed in NMR tubes. Magnetic gradient pulses are applied to label and read spin states to determine signal loss that occurs to molecular diffusion during some observation time. A 90° radiofrequency (rf) pulse aligns spins in the transverse (xy) plane, then a pulsed magnetic gradient is applied along the length of the sample, which labels the spins. Next, a 180° rf pulse induces a spin-echo in the xy -plane, followed by another magnetic pulse, and the spin-echo is read. The self-diffusion coefficient can be determined by fitting the spin-echo signal attenuation with the equation:⁹⁵

$$\frac{M(b)}{M_0} = e^{-\gamma G \delta^2 \left(\Delta - \frac{1}{3} \delta \right) D_{self}} \quad (14)$$

where M_0 is the net equilibrium magnetization in the z -direction, $M(b)$ is the magnetization in the z -direction as a function of b , where $b = (\gamma G \delta)^2 \left(\Delta - \frac{1}{3} \delta \right)$, G represents the amplitude of the field gradient pulses, δ is the pulse width, γ is the gyromagnetic ratio of the

Review Article

selected nucleus, Δ is the time period between gradient pulses, and D_{self} is the self-diffusion coefficient.

One significant benefit of the PFG NMR technique is that because diffusion is only measured in the direction of the magnetic field gradient, PFG NMR can be used to measure anisotropic diffusion in MOFs.⁹⁵ This has typically been accomplished by performing PFG NMR experiments with samples aligned in different crystal orientations⁹⁶ or fitting the data from powder samples with analytical solutions for self-diffusion tensors.⁹⁷ Forse et al. recently demonstrated that for nuclear spins that exhibit chemical shift anisotropy, the chemical shifts are dependent on crystallite orientation and anisotropic diffusion can be directly determined from the powder data.^{98,99}

Advances in the PFG NMR techniques, pulse sequences, and data analysis have improved the ability of PFG NMR to study transport in non-uniform systems. Diffusion-relaxation correlation spectroscopy DRCOSY experiments, which involve a PFG NMR spin-echo pulse sequence followed by a Carr-Purcell-Meiboom-Gill,¹⁰⁰ make it possible to simultaneously measure diffusion and T_2 relaxations and create correlational maps to determine whether a guest molecule's translational diffusion rate corresponds to its local mobility within the MOF pores. Hertel et al. performed DRCOSY measurements of benzene diffusion within MOF-5 and identified two distinct diffusion processes as transport through pristine pores and pores blocked by residual solvent.¹⁰⁰ Thoma developed a method for assessing guest diffusion through MOF powders with a wide distribution of crystal agglomerate sizes.¹⁰¹

In addition to PFG NMR, several other NMR techniques have been employed to evaluate molecular transport within MOFs. Li et al. performed a series of solid-state NMR experiments of light alkane diffusion in UiO-66. The diffusion of light alkanes in UiO-66 was examined by performing 2D ^1H - ^1H spin diffusion homonuclear correlation NMR experiments and tracking the increase in correlation intensity with time.¹⁰² Deuterium solid state NMR (^2H NMR) measurements of deuterated benzene confined in a perdeuterated UiO-66 MOF revealed the presence of anisotropic and isotropic powder patterns at low temperatures (Fig. 5). The anisotropic feature was attributed to benzene located within the smaller, tetrahedral pores of UiO-66, while the isotropic feature was attributed to benzene molecules in a mobile state in the octahedral pores. The anisotropic feature decreased with temperature and disappeared at $T > 193$ K, suggesting that benzene molecules can readily diffuse through the pores. The mechanism for benzene diffusion through UiO-66 was speculated to be a jump sequence involving benzene jumps between tetrahedral and neighboring octahedral pores. A diffusion coefficient based on the Einstein equation was in agreement with QENS data.¹⁰³

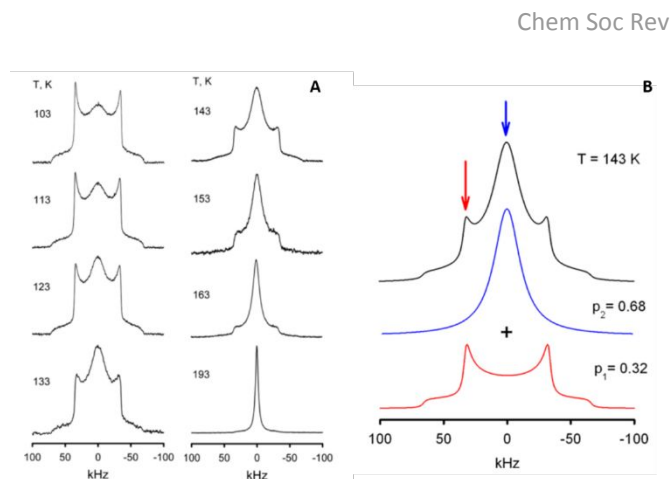


Fig. 5 Experimental ^2H NMR spectra of C_6D_6 in UiO-66 as a function of temperature (A) and simulation of ^2H NMR spectrum of C_6D_6 in UiO-66 at 143 K as a sum of two signals with an anisotropic (population p_1 , red) and isotropic (population p_2 , blue) patterns (B). Figure reproduced with permission from Kolokolov, D.I., Maryasov, A.G., Ollivier, J., Freude, D., Haase, J., Stepanov, A.G., Jobic, H., Journal of Physical Chemistry C, 2017, **121**, 2844, <https://pubs.acs.org/doi/10.1021/acs.jpcc.6b12001>. Copyright 2021 American Chemical Society. Notice: Further permissions related to the material excerpted should be directed to the ACS.

Infrared (IR) spectroscopy provides insight into the nature of the interactions between adsorbates and the surface by providing *in situ* information on the vibrational modes in the chemical environment of the sample. Infrared spectroscopy has been implemented as a technique to determine adsorption sites,^{54, 104} quantify binding strengths,⁵³ and understand molecular orientations of guest molecules within MOFs.⁵⁵ From Beer's law, the measured absorbance at a given frequency directly correlates to the concentration of the absorbed molecule. Each IR spectrum, therefore, provides a snapshot of the relative concentration of adsorbed molecules within a given MOF sample. Sharp et al. employed transmission IR to track the adsorption and diffusion of *n*-butane through a pelletized UiO-66 sample.⁴⁶ The decrease in intensity of the $\nu(\text{O-H})$ vibrational mode at 3675 cm^{-1} , attributed to the $\mu_3\text{-OH}$ groups on the zirconium nodes of UiO-66, corresponded to the formation of a broad band at 3641 cm^{-1} , indicating that *n*-butane adsorbed through weak hydrogen-bond formation with the zirconium node. To measure the diffusion, the decrease in vibrational modes assigned to adsorbed *n*-butane was used to track the relative concentration of butane over time (Fig. 6). The IR data were then fitted with a function derived from Fick's 2nd law of diffusion:

$$\frac{I_t}{I_0} = \theta \sum_{n=0}^{\infty} \frac{8}{(2n+1)^2 l \pi^2} e^{-\frac{D(2n+1)^2 \pi^2 t}{l^2}} \quad (15)$$

In Eq. 15, I_t represents the total integrated IR absorbance at time t , I_0 represents the total integrated IR absorbance at saturation coverage, θ represents the initial coverage at a given temperature, l represents the sample thickness, and D represents the diffusion coefficient. Grissom et al. utilized the same IR methods to investigate the diffusion of xylene isomers through UiO-66 and observed that despite an order of magnitude difference in measured diffusion coefficients at the same temperature, the activation energies of diffusion for each xylene isomer were approximately the same.⁴⁵ While quantitative IR diffusion experiments require a uniform sample thickness, transmission IR has also been utilized as a

qualitative tool to compare diffusion. Tan et al. measured the change in intensity of the $\nu(\text{C}\equiv\text{O})$ band attributed to adsorbed CO in Ni-MOF-74 over time and demonstrated that CO diffused more slowly when ammonia and water were co-adsorbed within the MOF.⁶⁷

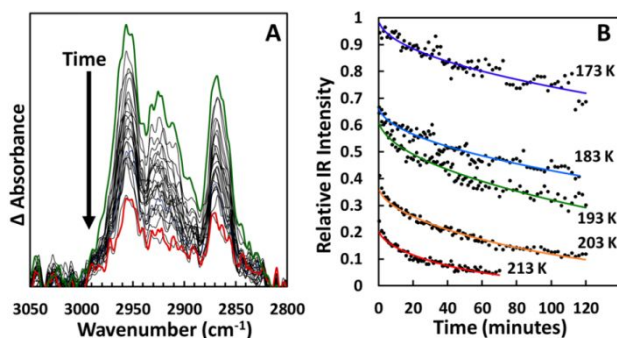


Fig. 6 Loss of IR intensity over time for n-butane through UiO-66 under ultrahigh vacuum conditions: (A) decrease in IR intensity for the C–H stretching region over time at 213 K; (B) change in IR intensity as a function of time at each temperature. The black dots are the experimental data, while the solid lines represent the Fickian diffusion model. Reprinted with permission from C. H. Sharp, J. Abelard, A. M. Plonka, W. Guo, C. L. Hill and J. R. Morris, *The Journal of Physical Chemistry C*, 2017, **121**, 8902-8906. Copyright 2021 American Chemical Society.

3.1.3 Microscopy Microscopic techniques, such as interference microscopy, IR microscopy, and fluorescence microscopy, allow for the measurement of transient guest-concentration profiles throughout a single MOF crystal with high spatial and temporal resolution.¹⁰⁵ The data gathered can be used to track the two-dimensional concentration profiles (**Fig. 7**) and resolve the contributions of surface permeability and intracrystalline transport diffusion to the overall mass transport of guest molecules.¹⁰⁶ The transport diffusion coefficient can be determined by fitting the concentration profiles along the length of a single crystal with an analytical solution for Fick's 2nd law of diffusion:¹⁰⁵

$$\frac{\partial C}{\partial t} = \frac{\partial}{\partial y} D_T \frac{\partial C}{\partial y} = \frac{\partial^2 C}{\partial y^2} + \frac{\partial D_T}{\partial C} \left(\frac{\partial C}{\partial y} \right)^2 \quad (16)$$

where t is time, D_T is the transport diffusion coefficient, C is concentration, and y is the position along the length of the crystal. An alternative approach is to consider the center of the crystal, where $\frac{\partial C}{\partial y} = 0$, and obtain the transport diffusivity from:

$$D_T = \frac{\partial C / \partial t}{\partial^2 C / \partial y^2} \quad (17)$$

In interference microscopy, the concentration of guest molecules diffusing through a MOF crystal is determined by measuring changes to its optical density. The incident light is split into two beams, one that passes through the crystal sample, and a reference beam that passes through the surrounding atmosphere. The patterns of each beam are superimposed on one another to generate interference patterns.¹⁰⁵ IR microscopy (IRM) combines the

temporal and spatial data of microscopy techniques and the molecular-level insight of infrared spectroscopy. Because IRM tracks changes to vibrational modes assigned to individual molecules, IRM has been employed to investigate mixture diffusion of small molecules in ZIF-8.⁶³ Similarly, the use of deuterated compounds can be used to perform tracer diffusion measurements to extract self-diffusion coefficients.⁶³ In addition to interference microscopy and IRM, fluorescence microscopy techniques, such as confocal fluorescence microscopy (CFM) and confocal laser scanning microscopy, have been employed to measure the transport diffusivity of fluorescent molecules in MOFs in the presence of a solvent.^{107, 108} Microscopy techniques require the synthesis of large single crystal MOF samples, typically on the micron to millimeter size scale.

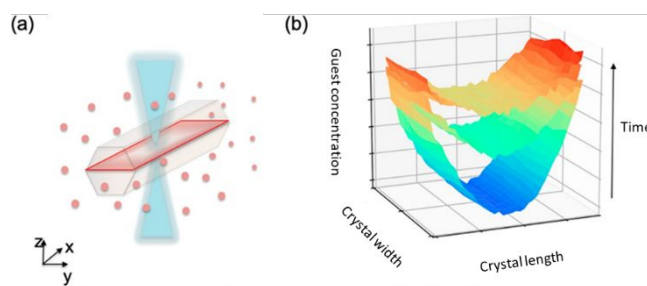


Fig. 7 (a) Schematic representation of a microscopy setup for monitoring guest diffusion within MOFs. (b) Time-resolved guest concentration map for guest diffusion through MOFs. Figure adapted with permission from R. Wang, B. C. Bukowski, J. Duan, T. R. Sheridan, A. Atilgan, K. Zhang, R. Q. Snurr and J. T. Hupp, *Langmuir*, 2020, **36**, 10853-10859. Copyright 2021 American Chemical Society.

3.1.4 Perspectives In the experimental measurement of guest diffusion through MOFs, each technique has its own inherent strengths and limitations. Spectroscopic methods allow for the measure of mass transport at small time- and length-scales, which is necessary for gaining mechanistic insight into the diffusion of molecules through MOFs, but some techniques such as QENS have stringent sample requirements (MOFs must be deuterated) and require access to specialized facilities or equipment. The development of microscopy-based techniques for measuring diffusion in MOFs provide temporally-resolved guest concentration maps that allow for the simultaneous quantification of guest diffusivity and surface permeability, but require large single MOF crystals. It is therefore important to employ multiple techniques or pair experimental methods with computational calculations to validate results.

An important caveat to keep in mind when comparing reported diffusivity values, however, is that variations in MOF sample and experimental conditions can lead to drastically different diffusion coefficients. In the case of CO₂ diffusion through MOF-5 at room temperature, Zhao et al. reported a diffusion coefficient of $7.9 \times 10^{-9} \text{ cm}^2 \text{ s}^{-1}$ while Saha et al. reported a diffusion coefficient of $1.17 \times 10^{-5} \text{ cm}^2 \text{ s}^{-1}$,^{82, 109} a four order-of-magnitude difference. Disagreements in measured diffusivities between different samples of the same guest-MOF system may be explained by a combination of differences in MOF samples (defect density, surface area, crystal size, activation

procedure), experimental conditions (guest concentrations, gas flow rates, pressures), or the choice of kinetic model for data fitting.

If possible, it is best to compare diffusion through MOF samples synthesized in the same batch under similar experimental conditions. In Kolokolov et al., the experimentally determined diffusivities for benzene in UiO-66 at 400 K using QENS and ^2H NMR were $3.3 \times 10^{-11} \text{ m}^2 \text{ s}^{-1}$ and $3.1 \times 10^{-11} \text{ m}^2 \text{ s}^{-1}$, respectively, demonstrating that strong experimental agreement between different techniques is possible when using the same MOF sample.¹⁰³ While it is not practical to only compare guest diffusivities using the same MOF samples, careful characterization of MOF samples and precise reporting of experimental conditions can help contextualize measured diffusivities and provide vital information to guide computational studies of mass transport in MOFs.

Similarly, when assessing molecular transport of different guest species within the same MOF, even subtle differences in the guest-guest and guest-MOF interactions due to chemical functionality and guest molecule size can have a profound effect on the diffusion rate. Fundamental research on chain-length, isomer and chemical substituent effects on mass transport in MOFs can help establish trends within a given MOF, but given the large number of possible guest molecules and MOF to investigate, these studies have been largely carried out using computational methods.

3.2 Techniques for Simulating Mass Transfer in Nanoporous Materials

The high crystallinity of many MOFs along with their modular design make them excellent model materials for improving our understanding of diffusion in nanoporous materials. In addition, with the proper choice of model, simulated diffusivities in MOFs can be accurately predicted in agreement with experimental measurements.¹¹⁰ In this section we describe the common techniques used to generate MOF crystal structures and describe the most popular force field choices for simulating diffusion. We then examine how equilibrium and non-equilibrium molecular dynamics simulations can be used to predict self-diffusion coefficients as well as transport diffusion coefficients in MOFs. The application of kinetic Monte Carlo in conjunction with transition state theory to predict diffusion is also considered, as well as lattice Boltzmann methods. Along the way, we discuss the state of the art for these techniques and briefly cover some applications described in the literature. Finally, we provide our perspectives on new methods for diffusion simulations and future directions that could be explored.

3.2.1 Models for MOF frameworks and adsorbates Simulating diffusion processes in MOFs requires a model of the MOF structure and equations that describe the interactions between adsorbates and the MOF atoms and among adsorbate molecules. Often the MOF crystal structure is known from x-ray crystallography. For proposed or hypothetical materials, a crystal structure can often be generated computationally as described below. The equations that describe the energetic interactions, known as a force field, should include the dominant types of interactions, such as dispersion, repulsion, electrostatics, and chemisorption for the system of interest. There

have been many different types of models used to simulate diffusion in MOFs, and we summarize some of these models and provide criteria for selecting different models. Finally, we discuss new developments in MOF force fields.

Experimental MOF structures are typically deposited in the Cambridge Structural Database.¹¹¹ Sometimes, the atomic coordinates can be used directly in a molecular simulation. In many cases, however, there may be partial occupancies of some atomic positions, missing hydrogen atoms, included solvent molecules, or other disorder that requires further processing to make the structure suitable as a simulation input. For an individual structure, this “clean up” can be done manually using various visualization tools. Recently, Chung et al. automated these procedures and provided over 14,000 MOFs structures in their Computation-Ready, Experimental MOF (CoRE MOF) Database.¹¹² Fig. 6 shows some of the processing steps the CoRE MOF Database uses to clean experimental structures. It should be noted that these automated cleaning steps are not perfect, and researchers should carefully analyze structures of particular interest.¹¹³

If the crystal structure for a given MOF is not available, there are now multiple algorithms for generating MOFs. By combining modular building blocks of metal clusters and organic linkers, Wilmer et al. were able to construct 137,953 MOFs, which they compiled in their hypothetical MOF (hMOF) database.¹¹⁴ The construction method used to create the hMOFs can also generate experimentally synthesized MOFs like HKUST-1 and MIL-47. Colon et al. used an alternative approach to MOF structure generation by using a top-down construction based on different underlying topologies.¹¹⁵ Using this approach, 13,512 MOFs were created, spanning 41 topologies. This Topologically Based Crystal Constructor (ToBaCCo) algorithm can be used to create MOFs when the nodes, linkers, and topologies are known. This algorithm has been extended to a larger space of possible topologies with ToBaCCo 3.0 developed by Anderson and Gómez-Gualdrón.¹¹⁶ Other construction algorithms have been developed, such as the graph theoretical approach from Boyd and Woo that extend the space of possible MOFs for different types of underlying topologies.¹¹⁷

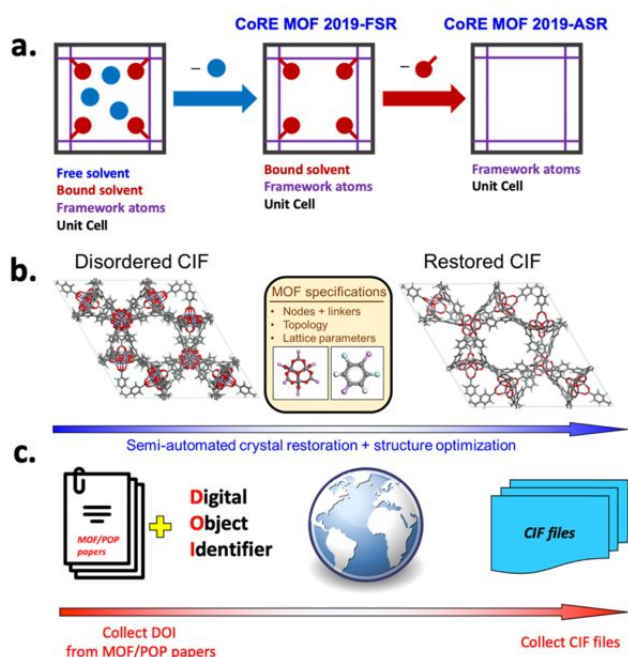


Fig. 8 Schematic of how the Computation-Ready Experimental Metal-Organic Framework Database (CoRE MOF Database) processes MOF structures. a) removing solvent molecules, b) fixing structural disorders. c) collating structures from the literature. Figure reproduced with permission from Chung, Y.G., Haldoupis, E., Bucior, B.J., Haranczyk, M., Lee, S., Zhang, H., Vogiatzis, K.D., Milisavljevic, M., Ling, S., Camp, J.S., Slater, B., Siepmann, J.I., Sholl, D.S., Snurr, R.Q., *Journal of Chemical & Engineering Data*, 2019, **64**, 5985-5998, <https://pubs.acs.org/doi/10.1021/acs.jced.9b00835>. Copyright 2021 American Chemical Society. Notice: Further Permissions related to the material excerpted should be directed to the ACS.

Once a suitable MOF structure has been obtained either through experimental crystallography or from a computational construction algorithm, it is necessary to determine the interatomic potentials or force field, including whether the framework is to be kept rigid or allowed to move. If framework motion can be neglected, the Universal Force Field (UFF) and DREIDING Force Field (DFF) are often used to model dispersion and repulsion interactions for framework atoms.^{118, 119} For example, such a model has been shown to predict self-diffusivities for C_1 to C_{16} n-alkanes in IRMOF-1 in good agreement with results from PFG NMR spectroscopy, with diffusivities spanning two orders of magnitude.^{94, 120, 121} If MOF flexibility is important (for example in MIL-53(Cr), which exhibits breathing modes that affect pore sizes), bond stretching, bending, and torsion terms must also be included in the MOF force field in addition to dispersion and repulsion terms.¹²² The development of accurate force fields that include framework flexibility is an active area of current research, and the review by Heinen and Dubbeldam provides a good overview of their construction.¹²³ In many cases, these force fields are parameterized using quantum chemistry techniques to reproduce physical properties such as binding energies, vibrational frequencies, unit cell size, and elastic properties like the bulk modulus. One of the force fields incorporating framework flexibility that have been used for diffusion simulations is QuickFF developed by Vanduyfhuys et al.^{124, 125} An advantage of Quick FF is that it can be used to generate force field parameters from quantum chemical calculations of the nodes and linkers to

efficiently generate force fields for different MOFs. Addicoat et al.¹²⁶ and Coupry et al.¹²⁷ have extended parameters from UFF to many of the metal nodes prevalent in MOFs to create the UFF4MOF force field. An advantage of UFF4MOF is that it can be immediately applied to many MOFs.

Electrostatic interactions between the MOF and adsorbates may be significant, for example for polar adsorbates. Atomic partial charges for a given MOF can be calculated using quantum chemistry calculations, and this is the preferred method when it is feasible. The quantum calculations can be performed on nodes and linkers separately or using the full periodic system. If quantum chemical calculations are prohibitively expensive, for example large unit cells or a very large number of MOFs to be considered, more approximate methods are sometimes used, especially variants on the charge equilibration method.¹²⁸⁻¹³¹ Recently, to speed up the assignment of partial charges to MOFs, machine learning methods have been developed that quantify the local chemical environment around each atom and predict its partial charge. Kancharlapalli et al. have developed a fast and accurate machine learning algorithm, trained on results from quantum chemical calculations, for calculating MOF partial charges using only the crystal structure.¹³² Korolev et al.¹³³ and Raza et al.¹³⁴ have also used data science approaches to accelerate the calculation of MOF partial charges. These methods may be amendable for situations where numerous MOFs are being studied for diffusion. The Quick FF and UFF4MOF force fields described previously also include partial charges in their formulation.

Accurate force fields for the adsorbates are also important for simulations, and depending on the type of adsorbate there are many force fields that have been used for diffusion simulations. For alkanes, the Transferable Potentials for Phase Equilibria (TraPPE) force field uses explicit atom types and also united-atom variants with CH_x pseudoatoms to model adsorbates.¹³⁵ This force field has been extended to alcohols,¹³⁶ aromatics,¹³⁷ fluoroalkanes,¹³⁸ and even organophosphate nerve agents and simulants,¹³⁹ among others. The Optimized Potentials for Liquid Simulations (OPLS) force field by Jorgensen is another commonly used force field for simulating organic adsorbates.¹⁴⁰

If the MOF structure is not prohibitively large, it may be possible to eschew a force field entirely and calculate diffusivities using ab initio MD, where the energies and forces are calculated using quantum chemical methods at each time step of the simulation. This may be preferable in situations where strong chemisorption, dynamic polarizability, or complex framework flexibility effects are important. In all cases, a quantum chemical approach will be slower than a force field due to the additional electronic degrees of freedom that must be calculated using a quantum Hamiltonian. The difference in CPU time for using a quantum chemistry approach will depend on the precise implementation used, but typically a quantum calculation will be orders of magnitude slower than using a force field. We can compare the limitations of these methods by their typical time and length scales. Force field MD simulations can reach tens of thousands of atoms and span up to multiple microseconds. Ab initio MD simulations are typically a few hundred atoms at a duration of 10s to 100s of picoseconds. Both techniques can be parallelized to

efficiently utilize multiple CPUs, and many codes can now use graphical processing units (GPUs). Even when using a quantum chemical approach, certain choices and approximations are still required, and we refer the interested reader to reviews on choosing quantum chemical methods in nanoporous materials.^{141, 142}

Most simulations of diffusion in MOFs consider “ideal” structures from x-ray diffraction or crystal structures generated on the computer and consider only diffusion in the interior of the crystals. However, defects and surface terminations may have a significant effect on the diffusivities. For example, Han et al. showed how simulated point defects in ZIF-8 increase hopping rates leading to higher adsorbate diffusivities.³⁰ Heinke et al.³¹ and Wang et al. have shown experimentally that surface barriers to diffusion are present in many MOFs and may be due to the MOF surface structure.¹⁰⁸ In situations where defects or surface terminations are important, the crystal structure must be modified. In these cases, comparisons with experimental structures or additional stability calculations may be required to determine reasonable models.

3.2.2 Diffusivities obtained from molecular dynamics simulations

Molecular dynamics (MD) simulations provide a direct approach for studying diffusion in nanoporous materials and calculating diffusion coefficients, as MD is similar in spirit to how an experiment would be carried out. In an MD simulation, adsorbates may be placed within a MOF and allowed to move according to the forces that they feel over time. If the system is at equilibrium, one can track the positions of individual adsorbates and obtain the self-diffusivity from the particle mean-squared displacements. The first molecular dynamics simulations were performed by Adler and Wainwright in 1957,¹⁴³ and this technique has been used extensively in the diffusion literature. In a molecular dynamics simulation, the forces acting on each atom are calculated from the potential energy (obtained from the force field), and Newton’s equations of motion are integrated numerically over many small time steps to obtain the molecular trajectories.¹⁴⁴

At sufficiently long times, molecules may exhibit a random walk, where the mean-squared displacement (MSD) is proportional to time (t). For a molecule diffusing without an external concentration gradient, we can obtain the self-diffusivity of component i using the Einstein relationship:

$$D_{s,i} = \lim_{t \rightarrow \infty} \frac{[\mathbf{x}_{l,i}(t) - \mathbf{x}_{l,i}(0)]^2}{6t} \quad (18)$$

where the position of molecule i is represented by the 3-dimensional vector \mathbf{x} . The self-diffusion coefficient can be computed by taking the slope at long times (when the mean-squared displacement is linear) of the mean-squared displacement versus time. We can average over each molecule of the system to reduce statistical fluctuations:

$$D_{s,i} = \lim_{t \rightarrow \infty} \frac{1}{6t} \left\langle \frac{1}{N_i} \sum_{l=1}^{N_i} [\mathbf{x}_{l,i}(t) - \mathbf{x}_{l,i}(0)]^2 \right\rangle \quad (19)$$

where N_i is the total number of molecules of species i . To obtain a reliable self-diffusion coefficient, the simulation time must be sufficiently long to ensure that molecules are diffusing and not

simply vibrating near their initial positions. It is strongly recommended to inspect MSD plots to investigate the slopes in different regions of the plot. Molecules may exhibit a ballistic region free from collisions, a subdiffusive regime characterized by collisions with walls, and finally a true diffusive regime as shown in Fig. 9. If the MSD is plotted on a log scale, it is straightforward to evaluate the diffusion mechanism at different times from the slopes of the plot. Vargas and Snurr developed an algorithm using Markov chain Monte Carlo to automatically fit each segment of the MSD and determine when the true diffusive regime begins.¹⁴⁵ Bukowski and Snurr used this algorithm to efficiently calculate self-diffusivities for 40 different MOFs without manual selection of the diffusive part of the MSD plots.¹⁹

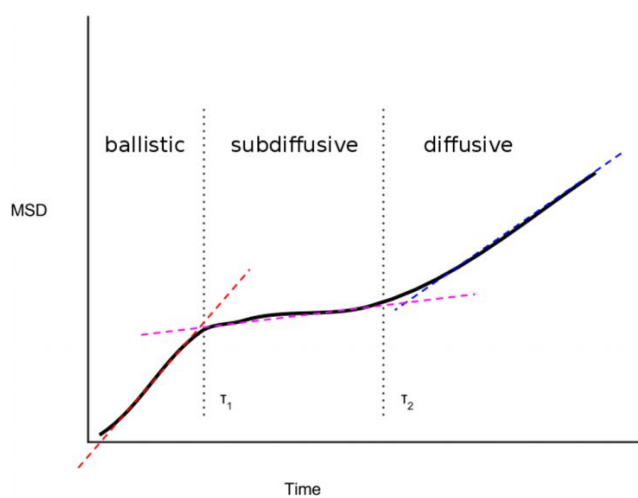


Fig. 9 Illustration of different slopes in the MSD plot that represent different transport mechanisms that may occur in MOFs. Reprinted with permission from E. Vargas L. and R. Q. Snurr, *Langmuir*, 2015, **31**, 10056-10065. Copyright 2021 American Chemical Society.

Statistical errors in the MSD plot can be large if the number of adsorbates is small. One solution is to perform multiple simulations using different initial positions or velocities, but it is also possible to look at different parts of the trajectory at different time origins to calculate the MSD. If we track a single molecule for a period of 10 ns, we would normally obtain a single MSD for that molecule. However, we could take the molecule’s position at, say, 1 ns as a new time origin to calculate a second MSD with a duration 9 ns in addition to the original MSD. In this way, we can perform a single longer MD simulation and average the MSD over multiple reference time origins to reduce statistical fluctuations. One must be careful that the different time origins are spaced significantly far enough apart that the trajectories are uncorrelated. For a detailed derivation of this algorithm, we recommend the work of Savin and Doyle.¹⁴⁶

So far, we have focused on modeling the self-diffusion of adsorbates using equilibrium MD simulations, i.e., in the absence of a concentration gradient. The self-diffusivities from such simulations can be compared with experimental techniques that measure self-diffusion, such as PFG NMR and QENS. Many experimental diffusion studies occur in the presence of a concentration gradient and focus on the transport or Fickian diffusivities. There are two general

approaches for calculating transport diffusivities from simulation: using either non-equilibrium molecular dynamics (NEMD) or equilibrium molecular dynamics (EMD). Each technique has its advantages and drawbacks, and we describe each of them briefly.

The NEMD approach to calculating transport diffusivities (D_T) is conceptually similar to what is done in an experimental diffusion measurement that includes a concentration gradient. As an example, we can construct a simulation box divided into two halves: one with adsorbates and the other without. Maginn et al. developed a technique where the concentration gradient in one dimension is monitored as the adsorbates diffuse from their non-equilibrium starting positions.¹⁴⁷ NEMD can also be used to look at diffusion through the surfaces of a MOF. In these simulations, one half of the simulation box initially contains a bulk fluid of adsorbates at equilibrium, and the other half of the box initially contains the empty MOF. At time 0 the divider is removed, and the bulk fluid diffuses into the MOF to reach a new equilibrium. One can directly calculate the flux of gas into the MOF by counting the number of molecules crossing a slice of the MOF per unit time,

$$J = \frac{N^{LR} - N^{RL}}{tA} \quad (20)$$

where the flux J is determined from the number of molecules N crossing a plane from the left to right (LR) or right to left (RL) of the MOF with area A during the time t . If we know the flux across a slice of the MOF, and we know the applied concentration gradient, the transport diffusivity can be calculated from Fick's first law. Velioglu and Keskin simulated H_2/CH_4 mixture permeation using this approach.¹⁴⁸

One drawback to the NEMD approach to calculating transport diffusion is that large simulation boxes and specialized algorithms are required to effectively extract a diffusion coefficient. This approach is prone to statistical fluctuations if the simulation box and number of molecules are small, requiring a larger system size or multiple simulations. In the case of simulating diffusion into a crystal, this also requires a model for the MOF surface, and the most stable surface termination and surface structure of the MOF may not be known.

Transport diffusivities D_T can also be derived from EMD simulations using the following equation, written in terms of the so-called corrected diffusivity D_C and the adsorption isotherm:

$$D_T = D_C \left(\frac{\partial \ln(f)}{\partial \ln(C)} \right)_T \quad (21)$$

Here f is the fugacity, C is the adsorbate concentration, and T is the temperature. The second factor is the log-derivative of the inverse adsorption isotherm. The adsorption isotherm can be obtained using simulation techniques such as grand canonical Monte Carlo. The corrected diffusivity can be obtained from the EMD simulation using the following expression:

$$D_{C,i} = \lim_{t \rightarrow \infty} \frac{1}{6t} \left\langle \left[\frac{1}{N_i} \sum_{l=1}^{N_i} x_{l,i}(t) - x_{l,i}(0) \right]^2 \right\rangle \quad (22)$$

The sum in equation 22 in comparison to equation 19 indicates that we are now measuring a collective diffusion of all adsorbate molecules as opposed to individual adsorbate motion. In the limit of low adsorbate loading, the log-derivative term in equation 21 goes to 1, and the transport and corrected diffusivities coincide. In fact, at low loadings the self-diffusivity also coincides with the corrected diffusivity, and all three diffusion coefficients are equal. In general, all three diffusion coefficients may depend on the adsorbate concentration. In the EMD approach, since one must average over all adsorbates to obtain a collective diffusivity, there can be considerable statistical noise in the MSDs, requiring long simulation times and/or multiple independent simulations that are averaged together. Both EMD and NEMD methods for obtaining transport diffusivities require more care and more computational resources than MD simulations for calculating self-diffusivities, which may be one reason that most studies report self-diffusion coefficients.

3.2.3 Calculating diffusion coefficients from transition-state theory

As noted above, MD simulations must be run long enough that the molecules have a measurable displacement on the time scale of the simulation. In general, it is recommended that the root-mean square displacement be larger than the unit cell length. With today's computing power, as a general heuristic, it is difficult to accurately calculate self-diffusion coefficients smaller than $\sim 10^{-11} \text{m}^2 \text{s}^{-1}$. For molecules that diffuse slowly due to their size, a low system temperature, or strong adsorption, MD simulations may not be able to access long enough simulation times to observe diffusive motion. Often in such systems, molecules move by a series of infrequent jumps between low energy adsorption sites. In this case, transition-state theory (TST) provides a way to estimate the rate for hopping between the adsorption sites. Given these rate constants, the self-diffusion coefficient can be estimated, as we briefly describe below. For example, alkanes in the MOF UiO-66 diffuse by hopping from one cavity to another by traversing the narrow windows that connect the cavities. If the potential energy surface $\mathcal{V}(\mathbf{x})$ is known (for example, from the same sorts of force fields used in MD simulations), the rate constant to move from state i (initial) to state j (final) can be written as:

$$k_{i \rightarrow j}^{TST} = \frac{kT \int_{x \in i} \delta[C(\mathbf{x})] |\nabla_{\mathbf{x}} C(\mathbf{x})| e^{-\beta \mathcal{V}(\mathbf{x})} d^v \mathbf{x}}{\int_{x \in i} e^{-\beta \mathcal{V}(\mathbf{x})} d^v \mathbf{x}} \quad (23)$$

where $\beta = (kT)^{-1}$, $C(\mathbf{x})$ is the dividing surface that separates states i and j , and $\delta[C(\mathbf{x})]$ selects for the dividing surface for the integral in the numerator. The TST rate constant assumes that all trajectories that reach the transition state thermalize in the final state j . To account for the possibility that some attempted transition events will recross back to the initial state or thermalize in another state, we can express the true hopping rate constant as:

$$k_{i \rightarrow j} = \kappa \times k_{i \rightarrow j}^{TST} \quad (24)$$

where κ is a dynamical correction factor that accounts for barrier re-crossings.¹⁴⁹

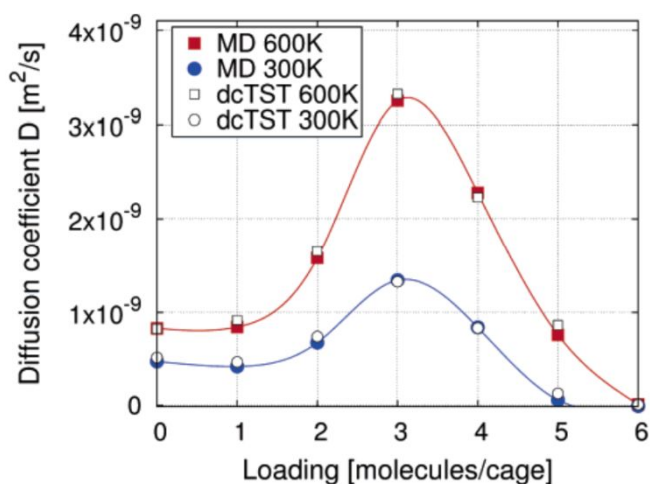


Fig. 10 Comparison between diffusion coefficients calculated using MD simulations and dynamically corrected transition state theory (dcTST) at two temperatures as a function of ethane loading in the cage-type zeolite CHA. Reprinted with permission from D. Dubbeldam, E. Beerdsen, S. Calero and B. Smit, *The Journal of Physical Chemistry B*, 2006, **110**, 3164-3172. Copyright 2021 American Chemical Society.

Calculating the rate constants for hopping between sites from TST requires that the Boltzmann factor be evaluated over the original state (to obtain the denominator) and over the dividing surface (to obtain the numerator). There are a variety of ways to do this. For example, Monte Carlo methods can be used to sample the potential energy surface. The Widom method randomly inserts test particles throughout the MOF and evaluates their energy, allowing one to sample the potential energy surface. The number of test particles inserted near the transition state will be small, so we need to bias the insertions to better sample this region of the potential energy surface. This may be performed using umbrella sampling, or other nonequilibrium free energy methods.¹⁴⁴ For example, Verploegh et al. used umbrella sampling to determine transition state rate constants for alkanes in ZIF-8.⁶⁵ Once $k_{i \rightarrow j}^{TST}$ is obtained, it is necessary to evaluate the dynamical correction factor κ that accounts for barrier re-crossing. This can be evaluated by starting MD simulations at the transition state and counting what fraction decay to the initial versus final state.¹⁴⁹

While we have briefly covered how to sample the potential energy surface and estimate the TST rate constants from **Eq. 23**, sometimes it is advantageous to determine the diffusion path for adsorbates. In some cases, this may be straightforward from examining the crystal structure, for example diffusion across the windows of UiO-66 or ZIF-8 are likely candidates for an activated hopping process. The potential energies of the initial and final states are straightforward to find due to their stability but obtaining the dividing surfaces is more difficult. Many of the techniques to find the minimum energy path require some form of biasing potential that will assist in selectively sampling the less stable configurations. One

popular technique for identifying a minimum energy path is the nudged elastic band (NEB) method from Mills et al.¹⁵⁰ and Henkelman et al.¹⁵¹⁻¹⁵³ that generates a hypothetical path between the initial and final states and evaluates the force tangent to images along the path using spring constants to converge on the transition state. In other situations, it may require numerous attempts at finding plausible diffusion paths to find the most favorable diffusion path. To accelerate the identification of diffusion paths, Mace et al. have developed an algorithm that identifies basins and tunnels in a nanoporous solid from the potential energy surface of the unit cell.¹⁵⁴ This enables automated high-throughput TST simulations for porous materials.

Once the hopping rate constants have been obtained using TST, the diffusion path must be identified. As an example, if the hopping rate constant and distance between the initial and final states (L) are known, and we assume a 1-D hop, the diffusivity can be calculated as:

$$D_{TST} = \frac{1}{2} k_{i \rightarrow j} L^2 \quad (25)$$

In general, $k_{i \rightarrow j} \neq k_{j \rightarrow i}$ because the potential energies of the initial and final states are different. Braun and Sholl developed a general theory to evaluate tensorial diffusion for any elementary periodic cell,¹⁵⁵ while Dubbeldam et al. have used sequential hops in different cage-type zeolites to calculate diffusion coefficients that agree with those calculated with molecular dynamics simulations as shown in **Fig. 10**.¹⁵⁶ For more complicated systems with multiple types of sites and different diffusion pathways, kinetic Monte Carlo can be used to predict the self-diffusion coefficient, given the connectivity of the sites, the relative probabilities of adsorbing in the sites, and the rate constants for hopping between each pair of connected sites. Kinetic Monte Carlo (kMC) stochastically propagates adsorbates among the sites according to their hopping rates in a coarse-grained model.^{157, 158} This allows the MSD to be computed without having to run an atomistic molecular dynamics simulation. In fact, self-diffusion coefficients obtained from TST+kMC and molecular dynamics can be directly compared and are equivalent if the MD is well-equilibrated, all relevant hopping coefficients have been included, and the approximations in TST are satisfied. The TST+kMC approach is especially useful for materials having cavities connected by narrow windows. In this case, the diffusivity obtained from a single hopping event may not capture the stochastic lateral motion between cages perpendicular to the diffusion axis. For such materials, we can consider the well-established n -fold algorithm by Bortz et al.¹⁵⁸ which allows molecules to hop between states for kMC. As an example of how kMC can be used with TST, Verploegh et al. compared TST+kMC, MD, and PFG NMR experiments to study water diffusion in ZIFs with mixed linker identities and found each technique agreed to within an order of magnitude as shown in **Fig. 11**.¹⁵⁹ In the Verploegh et al. model, there are 8 possible cages accessible from the current cage, and the probability of hopping to a given cage is proportional to the TST rate constant.

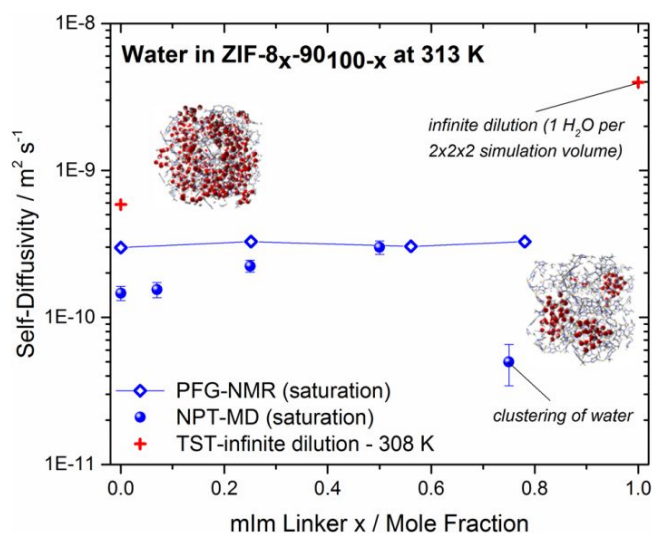


Fig. 11 Comparison between water self-diffusion coefficients calculated with molecular dynamics (NPT-MD), transition state theory (TST-infinite dilution), and experimentally measured PFG NMR. The MOF studied is a binary mixed-linker ZIF-8/ZIF-90. Reprinted with permission from R. J. Verploegh, Y. Wu, S. E. Bouffelfel and D. S. Sholl, *Journal of Physical Chemistry C*, 2018, **122**, 5627-5638. Copyright 2021 American Chemical Society.

Molecular dynamics simulations can be used with a biasing potential that appears in the Lagrangian such as Metadynamics as an alternative to locating transition states.¹⁶⁰⁻¹⁶² In Metadynamics, small biasing potentials are added to the Lagrangian of the system that slowly raises the energy of the initial state to move the adsorbate toward the transition state. This technique is especially useful for quantum chemical calculations where Monte Carlo methods are computationally infeasible. These techniques have been used in microporous zeolites with quantum chemical simulations.¹⁶³⁻¹⁶⁵ The Monte Carlo derived methods such as Widom insertion are not usually feasible with a quantum chemistry calculation, and it may be prohibitively time consuming to examine high molecular loadings. If the rate determining hopping event is known (for example, from a faster calculation using a force field) it may be possible to re-calculate the hopping barrier using quantum chemistry. This may be useful in situations where MOF flexibility is critical to providing an accurate prediction.

3.2.4 Lattice-Boltzmann Modeling Lattice-Boltzmann Modeling (LBM) was introduced three decades ago and has now been developed into a powerful tool for Computational Fluid Dynamics (CFD).^{166, 167} This method is particularly successful in fluid flow applications involving interfacial dynamics and complex boundaries¹⁶⁸. In the LBM, space is discretized into regularly distributed nodes on a lattice, and time is divided into evenly spaced intervals. Particle positions are confined to the nodes, and each node contains a particle population distribution in different directions that connects neighboring nodes.¹⁶⁹ Instead of directly solving the Boltzmann distribution, a nonlinear integral differential equation, the population distribution can be approximately solved by the discrete Lattice Boltzmann equation consisting of two steps at each time: 1) streaming, and 2) collision of the particles via the distribution function.

LBM has significant computational advantages since it is a mesoscopic lattice based model that is ideally suited for current

parallel computers. As a result, it can access much larger time scales than molecular dynamics methods and can be used to determine bulk properties, such as flow, diffusion, and permeability, properties that are critical to the design of MOFs. However, while the MOF structure can be represented exactly in the simulation, molecular details of the diffusing (or flowing) component cannot be included in this model. Rather, the LBM can model the transport properties of the center of mass motion of the molecule. Thus, it is better suited for smaller molecules rather than larger macromolecules. The inputs to the model include the structure of the MOF, the diffusion constant of the molecule in air/vacuum and if studying activated diffusion, the binding energies of the molecule to the MOF structure.

LBM has been adapted to study flow in nanoporous systems and studies have shown that LBM can be used to simulate a range of Knudsen numbers by incorporating the appropriate boundary conditions at the pore wall surface.¹⁷⁰ A study by Jiang et al¹⁷¹ applied LBM to study gas flow through an anisotropic MOF, for which they calculated permeability values in different flow directions. This method was applied to the NU-1000 MOF, but the basic approach was shown to work for a large class of MOFs as long as the spatial coordinates and sizes of MOF nodes and linkers are known. An example of the streamlines of gas flow through the UiO-66 MOF is shown in **Fig. 12**. As can be seen in the figure, regions of low and high flow velocity can be identified, the flux under different pressure gradients can be determined, and then by using Darcy's Law, the permeability can be calculated.

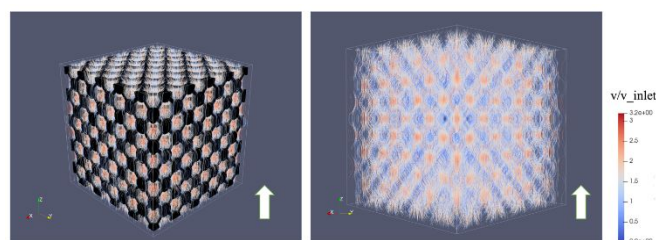


Fig. 12 A $10 \times 10 \times 10 \text{ nm}^3$ cubic view: streamlines of gas flow going through UiO-66 from direction $[0,0,1]$ (arrow direction). **Left:** streamlines shown with structure, with black spheres for MOF nodes and linkers. **Right:** the same streamlines shown without MOF structure. In both cases, the local velocity was scaled by the inlet velocity to better visualize the disturbance of flow.

LBM can also be used to determine the influence of the MOF structure on the diffusion coefficient by fitting diffusion profiles. As shown in **Fig. 13**, the same MOF in **Fig. 12** is initialized with a high concentration pulse (width $2h$, concentration C_0) at the center of the MOF. The pulse will then diffuse towards boundaries, and each timestep gives a diffusion profile, which can be fitted to the analytical solution of Fick's second law with infinite domain and extended initial condition, using diffusion coefficient D as fitting parameter to determine the time dependent diffusion coefficient. In these studies, the structure of the MOF only acts as a topological hindrance to diffusion, as there are no energetic interactions between the diffusing component and the MOF. These studies allow us to determine the role of the structure (topology) on the diffusion. Studies like this can then be used to estimate the extent of energetic interactions with the MOF structure by comparing it to experimental data.

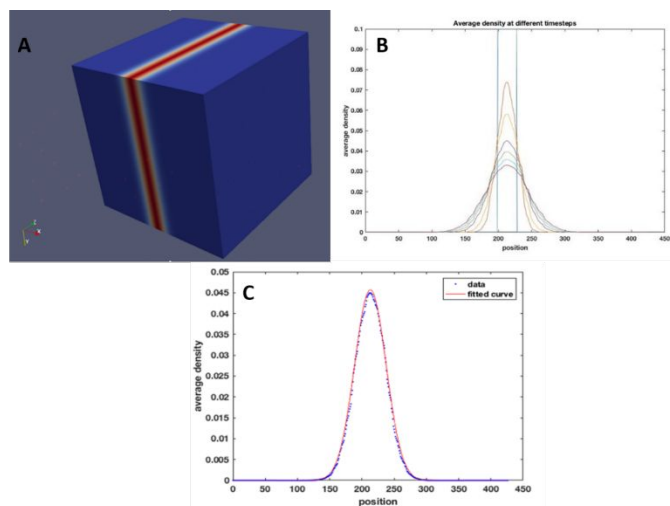


Fig. 13 Diffusion within a UiO-66 structure. (A) Initialization of a high concentration region at the center of the MOF. (B) Evolving concentration profiles as a function of time (C). Fit of the concentration profiles to the diffusion equation.

3.2.5 Perspective With increasingly robust structure generation and database efforts becoming more common, the design space of MOFs accessible to simulations continues to grow. Due to their crystallinity, there are many techniques available to researchers interested in adsorbate diffusion in MOFs. We have focused on techniques that integrate Newton's equations of motion (molecular dynamics) and those that sample the potential energy surface for diffusion (transition state theory). We have shown how these methods can be implemented, and depending on the system of interest, one may be easier than the other. While both techniques can be used to probe self-diffusion, MD can be used to simulate transport diffusivities due to an external concentration gradient using both EMD and NEMD. Recently, Chmelik and Kärger have shown how TST can be used with **Eq. 21** and additional approximations to predict the loading-dependent behavior of the transport diffusivity in ZIF-8.¹⁷²

The enormous number of hypothetical MOFs far exceeds the current capabilities of experimental synthesis. Chemical intuition about MOFs with favorable diffusion properties can be bolstered by high-throughput simulations that can test hypotheses about which MOFs produce the fastest adsorbate diffusion. While high-throughput gas storage calculations have become common, high-throughput diffusion studies are less common. MD simulations require long simulation times, and identifying the diffusive regime in the MSD plots is often done manually. Bukowski and Snurr have shown that by using automatic fitting of the MSD plot, it is possible to perform automated and high-throughput MD simulations.¹⁹ The algorithm developed by Mace et al. improves the usability of TST for high-throughput screening by automatically determining the diffusion paths and rate limiting transition states. The rate constants can then be used to perform kMC to calculate the diffusivity.¹⁵⁴ An example nanoporous solid considered by Mace et al. is shown in **Fig. 14**. Coupling these techniques with some of the available MOF databases, one could rapidly generate numerous adsorbate diffusivities. Rapidly obtaining transport diffusivities is more difficult, as both the equilibrium and non-equilibrium MD simulations to

obtain transport diffusivities are significantly more time-consuming than those used to obtain self-diffusivities.

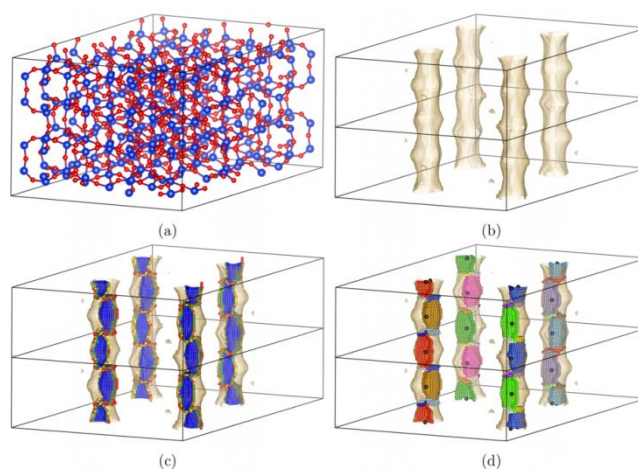


Fig. 14 Diffusion paths in the zeolite PSI automatically determined. A) PSI structure, B) potential energy isosurface, C) potential energies colored from lowest energy (blue) to highest energy (red). D) dividing surfaces colored uniquely, kMC grid points are black dots. Reproduced with permission from A. Mace, S. Barthel and B. Smit, *Journal of Chemical Theory and Computation*, 2019, **15**, 2127-2141, <https://pubs.acs.org/doi/10.1021/acs.jctc.8b01255>. Copyright 2021 American Chemical Society. Notice: Further Permissions related to the material excerpted should be directed to the ACS.

Most diffusion studies have focused on pristine MOF crystals, but surface terminations can also produce mass transport resistances that can dominate overall mass transport versus intracrystalline diffusion.³¹ In these cases, intracrystalline diffusivities may not be useful for predicting membrane or catalyst performance. These situations require close collaborations with experimental groups to first identify the rate-limiting mass transfer resistances and characterize the types of defects that may be present. In conjunction with experimental characterization, quantum chemistry calculations can be used to determine the relative stability of defects within MOF unit cells.

For some MOFs, the motion of the framework may significantly affect diffusion, either by changing the pore shape or window sizes.¹⁷³ Accurate force fields are required to accurately capture these effects, and the large MOF design space makes it difficult to develop highly accurate force fields that are transferable to the multitude of different MOF structures. Quantum chemical calculations are too computationally expensive to be performed on every MOF, but some level of QM may be required to fit interactions between nodes and linkers or to evaluate energies directly without a force field. QuickFF by Vanduyffhuys et al.^{124, 125} uses quantum chemistry to rapidly develop a MOF force field by performing efficient calculations on the nodes and linkers to then generalize an overall MOF force field. This method allows a force field to be generated even for exotic linkers and nodes that may have no existing force field. A significant advance would be the ability to determine whether a force field that includes framework flexibility is necessary for a given MOF, or whether a rigid model can be used

without loss of accuracy. A way of answering this question quickly for a given structure could dramatically increase the accuracy of diffusivity databases by making sure that each MOF is screened at the right level of force field accuracy.

4. Relevance of Mass Transport in Practical Applications of MOFs

4.1 Mass Transport in Electrochemically Active MOFs

MOFs have shown great promise in electrochemical systems due to what is considered a combination of homogeneous (e.g. high tunability, well-defined active sites) and heterogeneous (e.g. surface confined, high stability) properties.¹⁷⁴⁻¹⁷⁹ Electrochemical applications such as electrocatalysts, batteries, and electronics have all been proposed and explored with MOFs with much success.^{174-178, 180-186} To effectively perform electrochemical transformations in any system, it is necessary for electrons (from the electrode) and substrate (from the bulk solution) to all have sufficiently high diffusion rates in order to reach the active sites and perform the desired reactions. Optimization of electron and substrate diffusion rates is frequently considered for electrochemically active MOFs, but an often ignored aspect is the diffusion of counterions or electrolyte through the MOF pores.

The performance of electrochemical processes results in a large number of electrons moving throughout the MOF, resulting in multiple oxidation states. Therefore, diffusion of counterions is necessary to maintain electroneutrality.¹⁸⁷⁻¹⁸⁹ The slower of the diffusion rates between ions and electrons will be rate limiting, as an uncompensated electrical field will be generated due to fast movement of electrons or ions.¹⁸⁸ The electrical field will slow charge

carriers of the same charge and accelerate those of the opposite charge, helping to maintain the electroneutrality. The Scholz model can be used to visualize the movement of electrons and ions through an electrode-confined surface such as a MOF (Fig. 15a).¹⁸⁸ In this model, a three-phase boundary is proposed where the MOF surface, electrode, and bulk solution are all in contact. The electrons move between the electrode and MOF while ions diffuse between the MOF and bulk solution. As this boundary represents the shortest distance required for electrons, ions, and dissolved substrate to meet at an active site, electrochemical reactions are suggested to be largely surface confined at the start of electrochemical processes. Longer electrochemical experiments cause continued movement of electrons and counter-ions, which allow for propagation further into the MOF structure. Typical techniques for quantifying ion transport (i.e. electrochemical pulse-field-gradient spin-echo NMR)¹⁹⁰⁻¹⁹⁷ typically require much faster diffusion than is achievable in MOFs, but an electrochemical approach may not suffer the same limitation. The electroneutrality requirement presents a unique opportunity as electrons can be quantified electrochemically, and ion and electron movement are directly related in these systems.

Work from the Morris group shows one such effort to use electrochemistry to monitor ion diffusion in MOFs.¹⁸⁹ A zirconium-based MOF, NU-1000, was doped with three different metallocene species (Fe, Ru, or Os) to make use of the reversible redox features these metallocenes display. In conjunction with two different electrolyte species, tetrabutylammonium hexafluorophosphate (TBAPF₆) and tetrabutylammonium tetrakis(pentafluorophenyl)borate (TBATFAB), this work aimed to quantify electron diffusion (D_e) and ion diffusion (D_i) coefficients. Cyclic voltammetry (CV) in dichloromethane (DCM) provided electrochemical potentials for the one electron M^{2+}/M^{3+} redox event for each metallocene species. These potentials were then used as

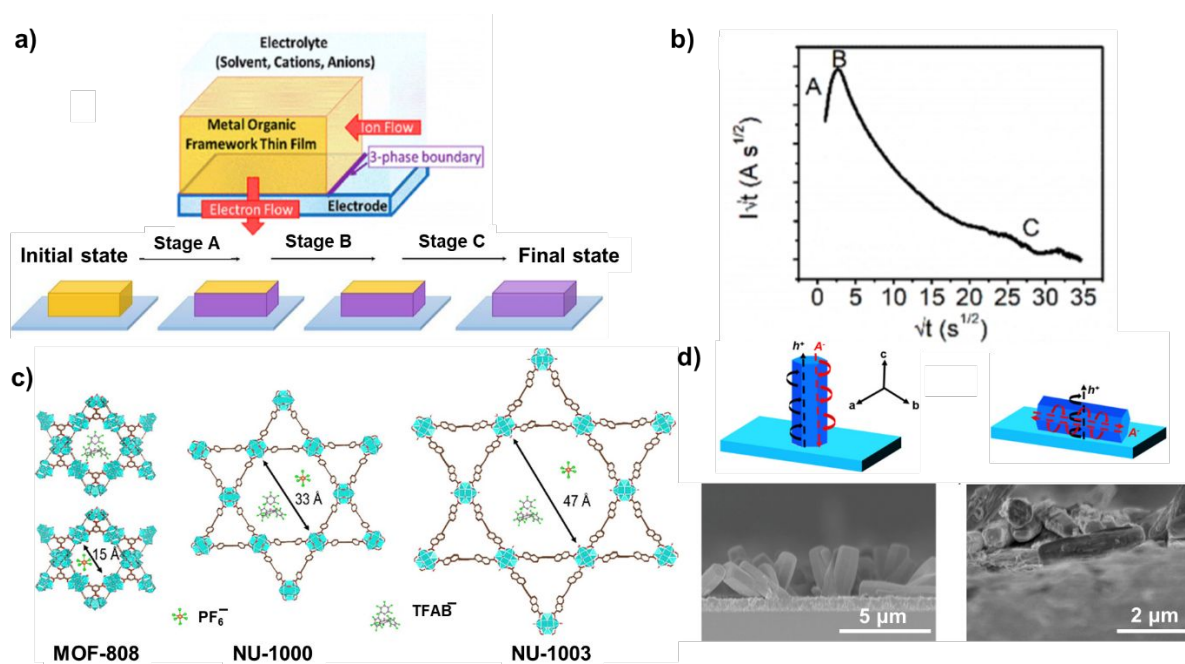


Fig. 15 Mass transport in electrochemically active MOFs: a) Scholz model for visualization of electron and ion movement through MOFs under applied bias, b) Chronoamperometric curve with different time stages, c) Size comparison between counter ion and studied MOF-808, NU-1000 and NU-1003, d) Illustration of NU-1000 MOFs prepared solvothermally and using electrophoretic deposition and corresponding SEM images. Figure adapted with permission from references 189 (Copyright 2021 American Chemical Society), 198 (Copyright 2021 American Chemical Society), and 200 (Copyright 2021 American Chemical Society).

guides for chronoamperometry experiments, where a constant electrochemical bias both lower (E_1) and higher (E_2) than the M^{2+}/M^{3+} couple is applied to observe the resultant current. Converting the current (I) vs time (t) data to $I\sqrt{t}$ vs \sqrt{t} , the plotted curves showed three regimes which were correlated to behavior proposed by the Scholz model (Fig. 15b). The first regime (A) showed an increase in the $I\sqrt{t}$ vs \sqrt{t} curve that can be interpreted as unimpeded electron and ion transport, suggestive of oxidation of the MOF surface. Regime B begins as the curve reaches a maximum and starts to decrease, where the surface of the MOF is completely oxidized and transport of electrons and ions into the bulk of the MOF takes over. Diffusion is limited by the slower of the two processes. The region where the curve approaches zero current represents the final regime (C), where nearly all of the metallocene species have been oxidized. Equations derived from the Scholz model were then used to quantify D_e and D_i . Comparison of the six metallocene-electrolyte combinations revealed that: (1) the D_e dependence on metallocene identity follows $Fe < Ru < Os$, behaving as would be expected based on self-exchange rates of the metallocenes; (2) D_i of TFAB⁻ was faster than PF₆⁻ despite TFAB⁻ being roughly 4 times the size of PF₆⁻ (TFAB_{vol} = 0.405 nm³, PF₆⁻_{vol} = 0.109 nm³) due to TFAB⁻ having lessened ion pairing with the metallocenes; and (3) ion diffusion was limiting in all cases as D_i was orders of magnitude lower than D_e . While a larger number of electrolyte and metallocene combinations may provide a more complete picture of the relationships between D_i , D_e , and electrochemical system, this work represents one of the first examples of quantifying D_i and D_e electrochemically within a MOF.

In a recent report, Morris et al. further explored the effect of different MOF structures on electron and ion diffusions (Fig. 15c).¹⁹⁸ Three zirconium-based MOFs (MOF-808, NU-1000 and NU-1003) with distinct pore sizes (15 Å, 33 Å and 47 Å, respectively), were post-synthetically decorated with ferrocene and studied using cyclic voltammetry and chronoamperometry in the presence of TBAPF₆ and TBATFAB electrolytes. Generally, the charge transport rates increased by a factor 10-100 when the MOF pore size increased from 15 Å to 47 Å. Deeper understanding of events that take place on a microscopic level was achieved using the Scholz model that revealed opposite trends for ion and electron diffusions. Ion diffusion occurred at a faster rate when diffusing through larger MOF pore sizes (from 10^{-14} to 10^{-12} cm²s⁻¹). For the largest pore MOF, Fc-NU-1003, the diffusion values for both electrolytes were almost equal (2.49×10^{-12} cm²s⁻¹ for PF₆⁻ vs. 2.17×10^{-12} cm²s⁻¹ for TFAB⁻), which suggests that the pore size was no longer a limiting variable for diffusion. Diffusion of electrons, however, exhibited a decrease by a factor of three with larger pore sizes as a direct consequence of electroactive species being further apart and, therefore, requiring greater hopping distances.¹⁹⁹ It should be noted that even for Fc-NU-1003, D_e values are still at least two orders of magnitude higher than ion diffusion, indicating that ion diffusion limits the overall charge transfer even when the pore size is >10 times bigger.

Another example of ion diffusion-limited charge transport was observed in a Hupp-Farha collaboration, where they studied the role of crystal orientation on charge propagation through MOFs.²⁰⁰ In their work, NU-1000 films were deposited onto an FTO-substrate using solvothermal synthesis and electrophoretic deposition. The two preparation methods yield different orientations in the films (Fig. 15d): solvothermal synthesis produces film that grows along the *c*-axis (perpendicular to the electrode), whereas electrophoretic deposition generates film with the crystallites parallel to the electrode (along the *ab*-plane). Electrochemical measurements on the two thin films with TBAPF₆ as the electrolyte revealed a stark difference between them; the overall charge transport rate was 300-

fold faster in solvothermally prepared NU-1000 films. Electrochemical impedance spectroscopy showed that the electrical conductivity (related to D_e) was improved by 100 times in *c*-oriented films due to the shorter hopping distances, indicating that an additional factor played a role in the improved charge-hopping rate. For solvothermal films, the electrolyte moves through the MOF channels in the same direction as redox hopping due to the directional growth of the MOF film. In electrophoretic-deposited films, the channels are orthogonal to the electron transport direction, which most likely slows down the overall charge hopping. The importance of the counterion was further highlighted by the sizable decrease (two to fourfold) in charge-hopping diffusion when sodium tetrakis[3,5-bis(trifluoromethyl)phenyl]borate was used as an electrolyte.

Electrochemical characterization of MOFs unveiled a unique dependence of charge transport on counter ion diffusion that is often inaccessible using other analytical methods. Results of cyclic voltammetry and chronoamperometry showed that the ion diffusion constants are often several orders of magnitude lower than electron diffusion and, thus, limit the overall charge transport even when MOF pore sizes are sufficiently large. Such observations invoke the necessity for a deeper understanding of processes that take place within the pores under applied external bias. With the latest advances in *in operando* techniques, such as small-angle neutron scattering,²⁰¹ we anticipate that the molecular-level understandings of electrochemical processes within MOFs will help develop more efficient electroactive systems.

4.2 Separations

The separations of chemical mixtures into pure components are a significant focus of the chemical industry and are energy and cost-intensive processes. It is estimated that 10-15% of the world's energy consumption is attributed to chemical separations, approximately half of which is due to distillation techniques.^{202, 203} New methods to efficiently separate molecules, especially under ambient temperatures, can provide a cost-effective and more environmentally-friendly alternative. The development of MOFs for use as separation platforms has been extensively discussed and reviewed in several publications.²⁰⁴⁻²⁰⁸ The separation of mixtures with MOFs can be accomplished by several techniques, including: 1) molecular sieving, where guest molecules of a certain size are physically prevented from entering and diffusing through the pores of the MOF, 2) kinetic separations, where each mixture component diffuses through a MOF at a different rate, and 3) selective equilibrium adsorption, where the MOF is designed to selectively adsorb one or several components of the mixture. Below, we highlight how the control over guest diffusion into and through MOFs can be utilized to perform separations of several industrially-relevant mixtures.

4.2.1 BTX Separations Recent work has demonstrated that MOFs can be utilized to separate benzene/toluene/xylene (BTX) mixtures at room temperature by tuning MOF pore diameter and aperture size. Polyukhov et al. studied the separation of xylene isomers through ZIF-8 under pseudo-ambient temperatures and observed that the sample temperature had a profound effect on the separation efficiency.²⁰⁹ A ZIF-8 sample synthesized with 2,2,6,6-

tetramethylpiperidin-1-yl)oxyl) (TEMPO) radicals (TEMPO@ZIF-8) allowed for the use of electron paramagnetic resonance measurements to investigate the penetration of BTX molecules into the ZIF-8 pores. At 298 K, the effective aperture of ZIF-8 ($d_{298\text{K}}$) was determined to be $6.96 \text{ \AA} < d_{298\text{K}} \leq 7.26 \text{ \AA}$, which allows *p*-xylene (critical diameter = 6.62 \AA) to readily penetrate into the pores of the MOF, but severely restricts the uptake of *m*-xylene (critical diameter = 7.26 \AA) and inhibits *o*-xylene adsorption (critical diameter = 7.27 \AA). As temperature was increased to 333 K, the effective diameter ($d_{333\text{K}}$) increased to $7.26 \text{ \AA} < d_{333\text{K}} \leq 7.27 \text{ \AA}$, allowing for *m*-xylene to be separated from *o*-xylene with a 92% separation efficiency.

Grissom et al. employed infrared spectroscopy to investigate the adsorption and diffusion of perdeuterated BTX molecules in UiO-66 and found that BTX molecules adsorb within the tetrahedral pores of the MOF through weak hydrogen-bond-like interactions with the $\mu_3\text{-OH}$ groups on the zirconium oxoclusters.⁴⁵ By tracking the decrease of $\nu(\text{C-D})$ vibrational modes attributed to adsorbed BTX molecules over time, diffusion coefficients were calculated by fitting the data with a Fickian diffusion model. While the activation energies for diffusion of the xylene isomers were similar (43–44 kJ/mol), *p*-xylene diffused approximately 20 times faster than *o*-xylene and 2–3 times faster than *m*-xylene at similar temperatures. Benzene and toluene, which both have kinetic diameters smaller than the 6.5 \AA triangular pore apertures of UiO-66, diffused at the same rate, suggesting that the rate-limiting step for BTX diffusion was the passage of molecules through the pore windows and not the rupture of the intermolecular hydrogen bonds. This hypothesis was further supported by comparing the diffusivity of *p*-xylene through UiO-66 before and after dehydroxylation of UiO-66. Despite a significant increase in *p*-xylene diffusivity with the absence of hydrogen-bonding, the activation energy of diffusion for *p*-xylene showed little change (Fig. 16). This work demonstrated that BTX diffusivities through MOFs can vary greatly when the pore size of the MOF is similar to the size of kinetic diameters of the guest molecules, which can be exploited for separation purposes.

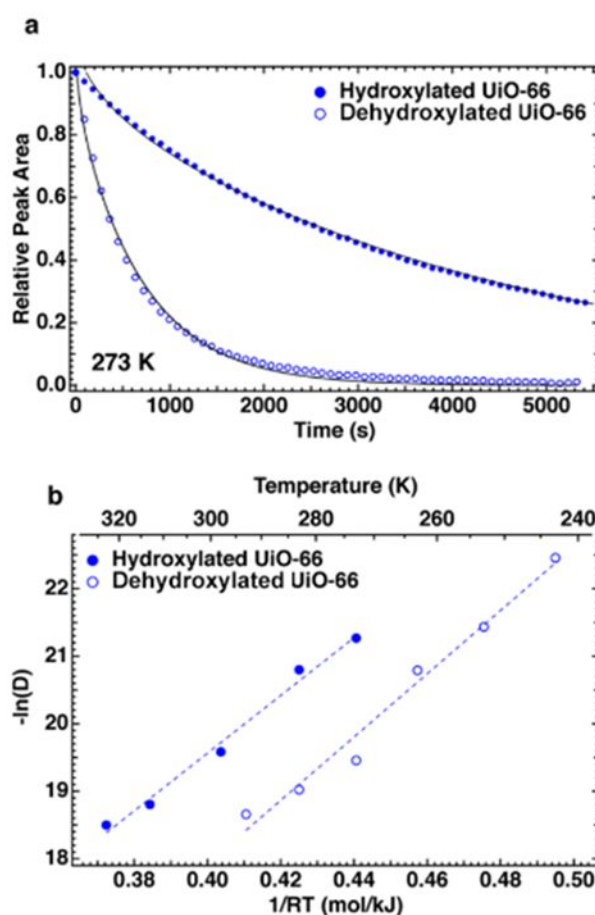


Fig. 16 *p*-Xylene- d_{10} diffusion through hydroxylated (solid blue) and dehydroxylated (outlined blue) UiO-66 at 273 K. The isothermal diffusion experiments were performed tracking the decrease in the $\nu(\text{C-D})$ vibrational modes attributed to *p*-xylene- d_{10} adsorbed within the UiO-66 sample. (a) Loss of relative IR peak area as a function of time (273 K). (b) Arrhenius plot based on a Fickian diffusion model. The activation energy of diffusion for *p*-xylene- d_{10} in dehydroxylated UiO-66 was determined to be $46.9 \pm 3.5 \text{ kJ mol}^{-1}$, similar to *p*-xylene- d_{10} in hydroxylated UiO-66 ($42.7 \pm 2.2 \text{ kJ mol}^{-1}$). Figure reproduced with permission from Grissom, T.G., Sharp, C.H., Usow, P.M., Troya, D., Morris, A.J., Morris, J.R., Journal of Physical Chemistry C, 2018, **122**, 16060.

Li et al. found that changing the metal center of MOF MFM-300(M) resulted in sub-angstrom changes to the diameter of the MOF's 1-dimensional zigzag channels and could tune the separation efficiency of xylene isomers at room temperature.²¹⁰ The synthesis of MFM-300(M) with M=In, V, Fe, and Al yielded MOFs with pore dimensions of 7.4, 7.0, 6.8, and 6.5 \AA , respectively. With the exception of MFM-300(Al), ternary breakthrough measurements and chromatographic separations of xylene isomers revealed that *p*-xylene eluted first, followed by *o*-xylene then *m*-xylene. Synchrotron-based X-ray diffraction measurements and terahertz spectroscopic studies of xylene isomer adsorption within the MFM-300(M) indicated that *m*-xylene bound most strongly within MFM-300(In), MFM-300(V), and MFM-300(Fe) through a combination $\pi \cdots \pi$ and Van der Waals interactions with the linkers of the MOF.

4.2.2 Alkane Separations The use of MOFs for the separation of alkanes and olefins has relied on a variety of techniques to

accomplish high separation efficiency at room temperature.²¹¹ Yu et al. demonstrated that MOF Al-bttotb can be used to separate C₆ isomers at room temperature by combining size-exclusion and kinetic separation methods.²¹² The 1D channels of Al-bttotb have a diameter of 5.6 Å that prevents the uptake of 2,2-dimethyl butane (kinetic diameter = 6.2 Å), separating it from the C₆ mixture through molecular sieving. Column breakthrough measurements revealed that 3-methyl pentane diffuses through Al-bttotb before n-hexane. DFT calculations determined that n-hexane adsorbs more strongly than 3-methyl pentane in the pores of Al-bttotb, resulting in a decreased diffusivity and increased retention times.

Wang et al. probed the effect of how pore topology affected the separation of C₆ alkane isomers within Zr-MOFs. Tetratopic linkers of similar length but different aspect ratios (the ratio between linker length and width) were used to create three Zr-MOFs with different node connectivities and pore topologies (Fig. 17).²¹³ The **ftw** (12-connected) and **scu** (8-connected) topologies, named compound **1** and **2**, respectively, both showed promise for the separation for C₆ isomers, with the **scu** topology outperforming the benchmark material zeolite 5A in column breakthrough experiments (the third MOF with an **lvt** structure (4-connected) was not thermally stable and therefore not tested).²¹³ For compound **1**, *ab initio* molecular dynamics calculations indicated that the narrow, 4.5 Å pore windows resulted in high diffusion barriers for 3-methylpentane and 2,3-dimethylbutane that significantly hinder diffusion into the pores of the MOF, resulting in a molecular sieving effect. For compound **2**, which has 1D channels ~7 Å in diameter, the separations were determined to be thermodynamically driven.

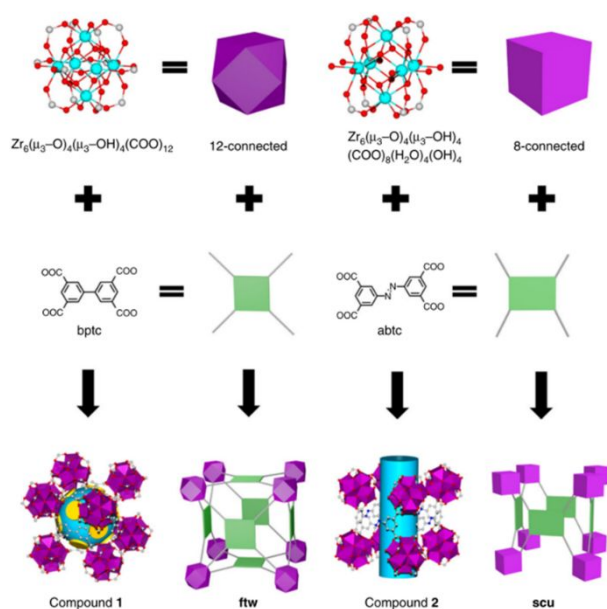


Fig. 17 Structural comparison of compounds **1** and **2**. Compounds **1** and **2** are built on 12- and 8- connected Zr₆ clusters, linked by tetratopic organic ligands bptc and abtc, forming **ftw** and **scu** type structures, respectively. Figure adapted with permission from Wang, H., Dong, X., Lin, J., et al., Nature Communications, 2018, 9, 1745.

Suh and Kim investigated the separation of hexane isomers in a ligand-inserted Mg-MOF-74 using MD simulations and observed that the insertion of 2,4-Di(4-pyridinyl)-1,3,5-triazine (dpt) ligands into the hexagonal channels of the MOF resulted in a reverse-shape selectivity.²¹⁴ Calculated diffusivities for 2,3-dimethylbutane and 2,2-dimethylbutane were approximately an order of magnitude faster than n-hexane. While n-hexane has the smallest kinetic diameter of the hexane isomers (4.3 Å), it has the largest maximum diameter (10.3 Å). It was speculated that the distance between the dpt ligands (8.3 Å) within the channels of Mg-MOF-74 sterically restricted n-hexane due to its length, hindering diffusion within the channel. Conversely, computed diffusivities of pentane isomers within the dpt-inserted Mg-MOF-74 decreased with increasing kinetic diameters.

4.2.3 Enantioselective Separations Recently, MOFs have emerged as a promising platform for the separation of racemic mixtures, which have significant importance in the biomedical and pharmaceutical industries. The synthesis of MOFs with homochiral ligands creates interior pore environments that preferentially adsorb certain enantiomers more strongly, resulting in stereoselective diffusivities.²¹⁵ The homochiral MOF TAMOF-1, containing L-histidine-based linkers, outperformed commercial columns for the separation of a racemic mixture of *trans*-2,3-diphenyloxirane.²¹⁶ Molecular dynamic simulations of ibuprofen and thalidomide enantiomer diffusion through TAMOF-1 revealed that the activation energies of diffusion vary for each enantiomer based on their adsorption geometry within the MOF. Moghadam and Düren performed GCMC simulations of the adsorption of racemic diol mixtures in Ni₂(L-aspartic acid)₂(4,4'-bipyridine) (Ni₂(L-asp)(bpy)) and observed R-enantioselectivity due to favorable guest-MOF interactions that allow for more efficient packing at higher loadings, which could result in slower diffusivity of R enantiomers.²¹⁷ In ZIF-8, the incorporation of chiral L- and D-histidine linkers enabled the MOF to separate racemic mixtures of tryptophan.²¹⁸

4.2.4 Perspectives The separation efficiency of MOFs can be controlled by a wide variety of parameters, including precise tuning of pore size and pore topology. Even sub-angstrom changes to the MOF structure can result in pronounced differences in guest diffusion of mixture components. Given the vast number of MOF structures that currently exist and more that are synthesized each year, experimentally-led investigations of guest diffusion through MOFs can act as a potential bottleneck for the development of MOF-based separation platforms. As mentioned in the section on computational methods, the use of computational structural libraries has provided a facile method for the high-throughput screening of MOF materials for separations. As of 2019, the Computation-Ready, Experimental Metal-Organic Framework Database (CoRE MOF Database) contains the structures of over 14,000 3-dimensional MOFs.¹¹² Chung et al. utilized the CoRE MOF database to screen 5109 MOFs for the separation of hexane and heptane isomers.²¹⁹ Li et al. used the CoRE MOF database to identify 15 MOFs out of over 5000 structures that trap CO₂ in the presence of

water.²²⁰ It should be noted that these computational screening efforts focused on differences in equilibrium adsorption, not differences in diffusion. Screening for materials that display kinetic selectivity is more difficult, as discussed above, but there are a growing number of examples in the literature.^{14, 148, 221-223} The continued development of these computational tools will enable faster identification of MOFs to be investigated for separation processes.

4.3 Heterogeneous Catalysis

Metal-organic frameworks have garnered significant attention for their use in heterogeneous catalysis.^{224, 225} The ability to tune the pore environment through linker and metal cluster choice can allow for the design of catalytic active sites that are tailored for the desired reaction. As Johnson et al. discuss,²²⁶ there is a fundamental need to understand the role of mass transport in kinetic studies of MOF-based catalysis to resolve the role of diffusion in the overall chemical reactivity, which besides a few studies,²²⁷ have been largely ignored. From Ernest Thiele's "reaction-diffusion" theory, catalysis within porous media can be either classified as diffusion-limited or reaction-limited.²²⁸ In the case of diffusion-limited reactions, where the diffusion rate is slower than the turnover rate for a given active site, catalysis is limited to the boundary layer of material. To realize the full potential of MOF-based catalysis, reactant diffusion rates must occur more rapidly than the catalytic turnover rate so that substrate molecules react at all available catalytic sites. It is therefore important to develop quantitative methods for analyzing the role of diffusion in catalysis. Several methods exist, such as kinetic modeling,²²⁹ isoreticular catalysis,²³⁰ kinetic isotope effects,¹³ and film-thickness/crystal size studies,²³¹ and are discussed more in-depth by Gao et al.¹³

A good example of the importance of active site accessibility and diffusion limitations in MOF-based catalysis is the hydrolysis of chemical warfare agents with Zr-based MOFs. UiO-66 was initially shown as a promising catalyst for the decomposition of nerve agent simulants (structural mimics) in buffered solutions, but reactions were limited to the surface of the crystallites due to the narrow triangular pore apertures (6 Å) of UiO-66.²³² Agrawal et al. performed molecular dynamics simulations to calculate the diffusion of the nerve agent sarin through UiO-66 and calculated a diffusion coefficient of $4.3 \times 10^{-13} \text{ cm}^2 \text{ s}^{-1}$ at 300 K, meaning it would take approximately 3 hours for a sarin molecule to diffuse through a 1 µm UiO-66 crystal.²³³ The use of UiO-67, which is isoreticular to UiO-66 but possesses longer linkers in the form of 4,4'-biphenyldicarboxylate, resulted in a decrease in the reaction half-life time by approximately an order of magnitude because internal active sites were more readily accessible.²³⁴ Further research into Zr₆-based MOFs has focused on changing the pore topology to both increase the number of coordinatively unsaturated Zr-sites and to facilitate faster molecular transport to catalyst sites within the MOF crystals to improve observed reaction rates.²³⁵

One way that scientists have mitigated mass transfer limitations in microporous MOF catalysts is through the use of hierarchically porous MOFs (HP-MOFs), which contain mesoporous (between 2 and 50 nm) channels that allow for enhanced diffusion of reactants to catalytic active sites. HP-MOFs can be generated through a myriad of different approaches, such as isoreticular expansion, defect-engineering, mixed-linker synthesis, surfactant-assisted synthesis, and hydrogel templating.^{236, 237} The synthesis of a hierarchically porous Cu-BTC MOF with the use of the anionic surfactant template sodium dodecylbenzene sulfonate created a HP-Cu-BTC with mesopores up to 24 nm, which showed improved conversion rates for the catalysis of the Henry reaction for 4-nitrobenzaldehyde.²³⁸ Qin et al. created a HP-MIL-101 MOF with a macroporous (larger than 50 nm) core and a mesoporous shell through selective etching which displayed an almost 4-fold increase in the conversion of 4-chlorostyrene to 4-chlorostyrene oxide compared to MIL-101.²³⁹

4.3.1 MOFs as Catalyst Supports MOFs have been successfully used for the encapsulation of catalysts, such as polyoxometalates (POMs),²⁴⁰⁻²⁴² metal nanoparticles,²⁴³ and enzymes,²⁴⁴ and other nanocatalysts.²⁴⁵ Given the breadth of literature on this subject, this section will only highlight a small portion of the literature on supported catalysts within MOFs. Encapsulation can offer protection from harsh chemical and thermal environments, limit catalyst sintering/leaching, and create well-dispersed catalytic sites. Nanocatalysts can be encapsulated in MOFs by a variety of methods,^{244, 246, 247} including synthesizing the MOF around the catalyst (*de novo* synthesis), post-synthetic infiltration of the synthesized catalyst, or synthesis of the catalyst within a pre-synthesized MOF. For encapsulated catalysts within MOFs, it is important to simultaneously restrict the transport of the catalyst material without drastically reducing the diffusivity of substrate molecules. This can be accomplished with the use of hierarchically porous MOFs, where the encapsulated catalysts are confined within smaller pores while the mesoporous regions enable rapid diffusion of reactants. In some instances, the catalysts can be confined within the mesopores of a MOF even when the pore diameter of the MOF exceeds the size of the catalyst, provided that strong intermolecular interactions between encapsulated catalysts and the pore walls of MOFs prevent leaching.²⁴⁸ For example, the Keggin POM H₅PV₂Mo₁₀O₄₀, which has a diameter of approximately 13 Å, was encapsulated within the mesopores of MIL-101(Cr) (diameter = 29-34 Å),²⁴⁰ Cu-BTC (diameter = 29.5 Å),²⁴⁹ and NU-1000 (31 Å).²⁴¹ The minimal changes in catalytic activity recyclability tests indicated that the POM successfully remained encapsulated in the MOFs.

In some instances, limiting active site accessibility and hindering reactant diffusion in MOF-based catalysis can be advantageous for controlling the selectivity of the catalytic reaction.²⁵⁰ Guo et al. observed that for Pt clusters confined within the pores of UiO-66-NH₂ (Pt@UiO-66-NH₂), the hydrogenation of cinnamaldehyde is selective for the aldehyde group as opposed to the alkene.²⁵¹ Given the small pore apertures of the UiO-66-NH₂, only the aldehyde can access the Pt inside the pores, enabling the selectivity. For Pt nanoparticles

encapsulated within MOFs ZIF-8 (Pt@ZIF-8), ZIF-67 (Pt@ZIF-67), and UiO-66 (Pt@UiO-66), citronellal is selectively hydrogenated to citronellol in Pt@ZIF-8 and Pt@ZIF-67 (Fig. 18).²⁵² The pore sizes for Pt@ZIF-8 and Pt@ZIF-67 are 3.4 Å and 3.3 Å, respectively, much smaller than the pores of Pt@UiO-66 (6 Å). Molecular dynamics simulations revealed that C=O group of citronellal preferentially penetrates the channels of ZIF-67 and ZIF-8 due to decreased steric interactions compared to the two methyl groups connected to the alkenyl group. Furthermore, the free rotation of the citronellal was hindered while diffusing through the ZIFs, limiting the ability for the alkenyl group to contact the Pt nanoparticles. While the restrictive diffusion through Pt@ZIF-8 and Pt@ZIF-67 resulted in a significantly lower turnover frequency as compared to the Pt@UiO-66 catalyst, they demonstrate that diffusion control through MOFs can allow for highly selective catalysis.

in MOFs will be especially important, as current techniques for quantitatively assessing multicomponent mixtures are limited.

5. Conclusions

The mass transport of molecules through the pores and channels of metal-organic frameworks is highly complex and dependent on several factors. The pore aperture and interior pore diameter of a MOF, which can vary depending on the linker dynamics and framework flexibility, limit which guest molecules can diffuse inside the MOF and can affect the guest-pore wall interactions. Binding sites, such as coordinatively unsaturated metal sites and Brønsted acid sites, can hinder diffusion by creating high activation energy barriers for site-hopping diffusion. The presence of defects and surface barriers, either intentionally synthesized or caused due to exposure to reactive conditions, can block channels and increase the tortuosity of diffusion.

Several experimental methods exist to measure guest diffusion within MOFs, but given the constraints and limitations of each technique, it is often useful to employ multiple techniques to assess diffusion at different length and time scales. Significant progress has been made in the development of computational methods to effectively calculate guest diffusivities in MOF structures, and with the advent of computational screening libraries, the ability to computationally study diffusion now significantly outpaces experimental measurements. Further research combining computational techniques and experiments will provide a clearer understanding of the role of defects and the importance of framework flexibility.

Understanding the complex nature of guest diffusion within metal-organic frameworks offers exciting potential for the continued development of MOFs for electrochemical applications, separations, and heterogeneous catalysis. In MOF-based catalysis, reducing MOF crystal sizes, synthesizing MOFs with hierarchical pore structures, and intentionally introducing defects can enable rapid substrate diffusion to allow reactions to occur at interior sites. In some instances, the restricted diffusion of reactants can allow for improved reaction selectivity and prevent unwanted side reactions. For catalysts encapsulated within MOFs, there must exist a balance between facilitating substrate diffusion while preventing catalyst leaching. Understanding the intermolecular guest-MOF interactions can allow scientists and engineers to tune experimental conditions, such as temperature and gas pressure, to optimize pore size for highly efficient separations.

Conflicts of Interest

There are no conflicts to declare.

Acknowledgements



Fig. 18 Schematic of selective hydrogenation of citronellal to citronellol catalyzed by platinum nanoparticles encapsulated within MOFs with different channel environments. Figure reproduced with permission from W. Zhang, W. Shi, W. Ji, H. Wu, Z. Gu, P. Wang, X. Li, P. Qin, J. Zhang, Y. Fan, T. Wu, Y. Fu, W. Zhang and F. Huo, ACS Catalysis, 2020, 10, 5805-5813. Copyright 2021 American Chemical Society

4.3.2 Perspectives Developing an understanding of how guest transport through MOFs affects both the kinetics and mechanisms of a catalytic process is critical for optimizing catalytic turnover rates and reaction selectivities. With the continued development of reported MOF structures with different pore domains, nanosized catalysts can be successfully encapsulated without blocking access to internal pores. The increase in synthetic approaches to develop MOFs with hierarchical pore structures has enabled traditionally microporous MOFs, such as UiO-66,²⁵³ to be developed as shape-selective catalysts while still ensuring rapid enough substrate diffusion to enable catalysis at sites deep within the crystals. Before we can realize the full capabilities of these catalysts, it is necessary to perform fundamental measurements of substrate and product diffusion through MOFs to develop kinetic reaction models. The development of *in operando* methods for assessing mass transport

This work is supported by the U.S. Army Research Laboratory and the U.S. Army Research Office under grant no. W911NF-20-2-0058. The views and conclusions herein are those of the authors and should not be interpreted as necessarily representing the official policies or endorsements, either expressed or implied, of the ARO, DOE, or the U.S. Government. This publication was written while Conor Sharp held an NRC Research Associateship award at the U.S. Naval Research Laboratory. Stefan Ilic was supported by the U.S. Department of Energy, Office of Science, Office of Basic Energy Sciences, under award DE-SC0012445. Eric Johnson was supported by the National Science Foundation under Grant No. 1551964. Brandon Bukowski and Randall Snurr acknowledge financial support from the Defense Threat Reduction Agency (HDTRA1-19-1-0007).

References

1. S. L. James, *Chemical Society Reviews*, 2003, **32**, 276-288.
2. C. Altintas, G. Avci, H. Daglar, A. Nemati Vesali Azar, I. Erucar, S. Velioglu and S. Keskin, *Journal of Materials Chemistry A*, 2019, **7**, 9593-9608.
3. H. Furukawa, K. E. Cordova, M. O'Keeffe and O. M. Yaghi, *Science*, 2013, **341**.
4. P. Saffman, *Journal of Fluid Mechanics*, 1959, **6**, 321-349.
5. J. Karger, Ruthven, D.M., Theodorou, D.N., in *Diffusion in Nanoporous Materials*, Wiley, 2012, ch. 1, pp. 1-24.
6. E. L. Cussler and E. L. Cussler, *Diffusion: mass transfer in fluid systems*, Cambridge university press, 2009.
7. Y. Mo, J. Kleiner, M. Webb and M. Lagally, *Physical review letters*, 1991, **66**, 1998.
8. Z. Zhao, Z. Li and Y. Lin, *Industrial & Engineering Chemistry Research*, 2009, **48**, 10015-10020.
9. Y. Wu, G. Cheng, K. Katsov, S. W. Sides, J. Wang, J. Tang, G. H. Fredrickson, M. Moskovits and G. D. Stucky, *Nature materials*, 2004, **3**, 816-822.
10. R. Krishna, *Chemical Society Reviews*, 2012, **41**, 3099-3118.
11. J. Karger, Ruthven, D.M., Theodorou, D.N., *Diffusion in Nanoporous Materials*, Wiley-VCH, Weinheim, 2012.
12. D. N. Theodorou, Snurr, R.Q., Bell, A.T., in *Comprehensive Supramolecular Chemistry*, ed. G. Alberti, Bein, T., Pergamon, Oxford, 1999, vol. 7, pp. 507-548.
13. W. Y. Gao, A. D. Cardenal, C. H. Wang and D. C. Powers, *Chemistry - A European Journal*, 2019, **25**, 3465-3476.
14. E. Haldoupis, S. Nair and D. S. Sholl, *Journal of the American Chemical Society*, 2010, **132**, 7528-7539.
15. K. Li, D. H. Olson, J. Seidel, T. J. Emge, H. Gong, H. Zeng and J. Li, *Journal of the American Chemical Society*, 2009, **131**, 10368-10369.
16. S. Amirjalayer and R. Schmid, *Journal of Physical Chemistry C*, 2016, **120**, 27319-27327.
17. A. C. Forse, K. A. Colwell, M. I. Gonzalez, S. Benders, R. M. Torres-Gavosto, B. Blümich, J. A. Reimer, J. R. Long, A. C. Forse, K. A. Colwell, M. I. Gonzalez, S. Benders, R. M. Torres-Gavosto, B. Blümich, J. A. Reimer and J. R. Long, *Chemistry of Materials*, 2020, **32**, 3570-3576.
18. T. M. Osborn Popp, A. Z. Plantz, O. M. Yaghi and J. A. Reimer, *ChemPhysChem*, 2020, **21**, 32-35.
19. B. C. Bukowski and R. Q. Snurr, *ACS Applied Materials & Interfaces*, 2020, **12**, 56049-56059.
20. Q. Yang, H. Jobic, F. Salles, D. Kolokolov, V. Guillermin, C. Serre and G. Maurin, *Chemistry – A European Journal*, 2011, **17**, 8882-8889.
21. N. A. Ramsahye, J. Gao, H. Jobic, P. L. Llewellyn, Q. Yang, A. D. Wiersum, M. M. Koza, V. Guillermin, C. Serre, C. L. Zhong and G. Maurin, *Journal of Physical Chemistry C*, 2014, **118**, 27470-27482.
22. D. C. Ford, D. Dubbeldam and R. Q. Snurr, in *Diffusion Fundamentals III*, eds. C. Chmelik, N. Kanellopoulos, J. Kärger and D. Theodorou, Leipziger Universitätsverlag, 2009, pp. 459-466.
23. S. Devautour-Vinot, G. Maurin, C. Serre, P. Horcajada, D. Paula da Cunha, V. Guillermin, E. de Souza Costa, F. Taulelle and C. Martineau, *Chemistry of Materials*, 2012, **24**, 2168-2177.
24. S. A. Moggach, T. D. Bennett and A. K. Cheetham, *Angewandte Chemie International Edition*, 2009, **48**, 7087-7089.
25. A. Gonzalez-Nelson, F. X. Coudert and M. A. van der Veen, *Nanomaterials*, 2019, **9**, 330-365.
26. M. Agrawal and D. S. Sholl, *ACS Applied Materials and Interfaces*, 2019, **11**, 31060-31068.
27. F. Salles, H. Jobic, A. Ghoufi, P. L. Llewellyn, C. Serre, S. Bourrelly, G. Férey and G. Maurin, *Angewandte Chemie International Edition*, 2009, **48**, 8335-8339.
28. A. Sławek, J. M. Vicent-Luna, B. Marszałek, B. Gil, R. E. Morris, W. Makowski and S. Calero, *Chemistry of Materials*, 2018, **30**, 5116-5127.
29. A. Knebel, B. Geppert, K. Volgmann, D. I. Kolokolov, A. G. Stepanov, J. Twiefel, P. Heitjans, D. Volkmer and J. Caro, *Science*, 2017, **358**, 347-351.
30. C. Han, R. J. Verploegh and D. S. Sholl, *Journal of Physical Chemistry Letters*, 2018, **9**, 4037-4044.
31. L. Heinke, Z. Gu and C. Wöll, *Nature Communications*, 2014, DOI: 10.1038/ncomms5562, 4562.
32. K. Müller, N. Vankova, L. Schöttner, T. Heine and L. Heinke, *Chemical Science*, 2019, **10**, 153-160.
33. Z. Fang, B. Bueken, D. E. De Vos and R. A. Fischer, *Angewandte Chemie International Edition*, 2015, **54**, 7234-7254.
34. S. Yuan, L. Zou, J.-S. Qin, J. Li, L. Huang, L. Feng, X. Wang, M. Bosch, A. Alsalme, T. Cagin and H.-C. Zhou, *Nature Communications*, 2017, **8**, 15356.
35. W. Xiang, Y. Zhang, Y. Chen, C.-j. Liu and X. Tu, *Journal of Materials Chemistry A*, 2020, **8**, 21526-21546.
36. S. Zhang, B. Gui, T. Ben and S. Qiu, *Journal of Materials Chemistry A*, 2020, **8**, 19984-19990.
37. R. A. Homan, D. S. Hendricks, T. M. Rayder, U. S. Thein, K. J. Fossum, A. P. Claudio Vázquez, J. Yan, R. L. Grimm, S. C. Burdette and J. C. MacDonald, *Crystal Growth and Design*, 2019, **19**, 6331-6338.
38. C. Xu, J. Yang, M. Veenstra, A. Sudik, J. J. Purewal, Y. Ming, B. J. Hardy, J. Warner, S. Maurer, U. Müller and D. J. Siegel, *International Journal of Hydrogen Energy*, 2013, **38**, 3268-3274.
39. J. J. Purewal, D. Liu, J. Yang, A. Sudik, D. J. Siegel, S. Maurer and U. Müller, *International Journal of Hydrogen Energy*, 2012, **37**, 2723-2727.
40. S. Krishnamurthy, R. Blom, M. C. Ferrari and S. Brandani, *Adsorption*, 2020, **26**, 711-721.
41. J. Liu, Y. Wang, A. I. Benin, P. Jakubczak, R. R. Willis and M. Douglas Levan, *Langmuir*, 2010, **26**, 14301-14307.

42. C. Zhang, J. A. Gee, D. S. Sholl and R. P. Lively, *Journal of Physical Chemistry C*, 2014, **118**, 20727-20733.
43. S. Tanaka, K. Fujita, Y. Miyake, M. Miyamoto, Y. Hasegawa, T. Makino, S. Van Der Perre, J. Cousin Saint Remi, T. Van Assche, G. V. Baron and J. F. M. Denayer, *Journal of Physical Chemistry C*, 2015, **119**, 28430-28439.
44. J. Zhu, J. Liu, Y. Machain, B. Bonnett, S. Lin, M. Cai, M. C. Kessinger, P. M. Usov, W. Xu, S. D. Senanayake, D. Troya, A. R. Esker and A. J. Morris, *Journal of Materials Chemistry A*, 2018, **6**, 22195-22203.
45. T. G. Grissom, C. Sharp, P. Usov, D. Troya, A. Morris, J. Morris, C. H. Sharp, P. M. Usov, D. Troya, A. J. Morris and J. R. Morris, *The Journal of Physical Chemistry C*, 2018, **122**.
46. C. H. Sharp, J. Abelard, A. M. Plonka, W. Guo, C. L. Hill and J. R. Morris, *The Journal of Physical Chemistry C*, 2017, **121**, 8902-8906.
47. J. J. Wardzala, J. P. Ruffley, I. Goodenough, A. M. Schmidt, P. B. Shukla, X. Wei, A. Bagusetty, M. De Souza, P. Das, D. J. Thompson, C. J. Karwacki, C. E. Wilmer, E. Borguet, N. L. Rosi and J. K. Johnson, *The Journal of Physical Chemistry C*, 2020, DOI: 10.1021/acs.jpcc.0c07040.
48. A. Liu, X. Peng, Q. Jin, S. K. Jain, J. M. Vicent-Luna, S. Calero and D. Zhao, *ACS Applied Materials & Interfaces*, 2019, **11**, 4686-4700.
49. A. Burgun, C. J. Coghlan, D. M. Huang, W. Chen, S. Horike, S. Kitagawa, J. F. Alvino, G. F. Metha, C. J. Sumbly and C. J. Doonan, *Angewandte Chemie International Edition*, 2017, **56**, 8412-8416.
50. Y. Inokuma, S. Yoshioka, J. Ariyoshi, T. Arai, Y. Hitora, K. Takada, S. Matsunaga, K. Rissanen and M. Fujita, *Nature*, 2013, **495**, 461-466.
51. M. Viciano-Chumillas, M. Mon, J. Ferrando-Soria, A. Corma, A. Leyva-Pérez, D. Armentano and E. Pardo, *Accounts of Chemical Research*, 2020, **53**, 520-531.
52. R. J. Young, M. T. Huxley, E. Pardo, N. R. Champness, C. J. Sumbly and C. J. Doonan, *Chemical Science*, 2020, **11**, 4031-4050.
53. T. G. Grissom, D. M. Driscoll, D. Troya, N. S. Sapienza, P. M. Usov, A. J. Morris and J. R. Morris, *The Journal of Physical Chemistry C*, 2019, **123**, 13731-13738.
54. D. M. Driscoll, D. Troya, P. M. Usov, A. J. Maynes, A. J. Morris and J. R. Morris, *The Journal of Physical Chemistry C*, 2018, **122**, 14582-14589.
55. D. M. Driscoll, D. Troya, P. M. Usov, A. J. Maynes, A. J. Morris and J. R. Morris, *Physical Chemistry Chemical Physics*, 2019, **21**, 5078-5085.
56. K. I. Hadjiivanov, D. A. Panayotov, M. Y. Mihaylov, E. Z. Ivanova, K. K. Chakarova, S. M. Andonova and N. L. Drenchev, *Chemical Reviews*, 2020, DOI: 10.1021/acs.chemrev.0c00487.
57. Y.-P. Xu, Z.-Q. Wang, H.-Z. Tan, K.-Q. Jing, Z.-N. Xu and G.-C. Guo, *Catalysis Science & Technology*, 2020, **10**, 1699-1707.
58. J. P. P. Ruffley, I. Goodenough, T.-Y. Y. Luo, M. Richard, E. Borguet, N. L. Rosi, J. Karl Johnson, N. L. Rosi and J. K. Johnson, *Journal of Physical Chemistry C*, 2019, **123**, 19748-19758.
59. P. Zhao, H. Fang, S. Mukhopadhyay, A. Li, S. Rudić, I. J. McPherson, C. C. Tang, D. Fairen-Jimenez, S. C. E. Tsang and S. A. T. Redfern, *Nature Communications*, 2019, **10**, 1-8.
60. F. Walenzus, V. Bon, J. D. Evans, S. Kaskel and M. Dvoyashkin, *The Journal of Physical Chemistry Letters*, 2020, **11**, 9696-9701.
61. F. Salles, S. Bourrelly, H. Jobic, T. Devic, V. Guillermin, P. Llewellyn, C. Serre, G. Ferey and G. Maurin, *Journal of Physical Chemistry C*, 2011, **115**, 10764-10776.
62. S. Wang, G. Zhou, Y. Sun and L. Huang, *AIChE Journal*, 2020, DOI: 10.1002/aic.17035.
63. C. Chmelik, *Microporous and Mesoporous Materials*, 2015, **216**, 138-145.
64. A. I. Skoulidas and D. S. Sholl, *Journal of Physical Chemistry B*, 2005, **109**, 15760-15768.
65. R. J. Verploegh, S. Nair and D. S. Sholl, *Journal of the American Chemical Society*, 2015, **137**, 15760-15771.
66. S. Bendt, Y. Dong and F. J. Keil, *Journal of Physical Chemistry C*, 2019, **123**, 8212-8220.
67. K. Tan, S. Jensen, S. Zuluaga, E. K. Chapman, H. Wang, R. Rahman, J. Cure, T. H. Kim, J. Li, T. Thonhauser and Y. J. Chabal, *Journal of the American Chemical Society*, 2018, **140**, 856-859.
68. B. Borah, H. Zhang and R. Q. Snurr, *Chemical Engineering Science*, 2015, **124**, 135-143.
69. J. Liu, S. Keskin, D. S. Sholl and J. K. Johnson, *Journal of Physical Chemistry C*, 2011, **115**, 12560-12566.
70. Y. Wang, *Adsorption*, 2021, **27**, 369-395.
71. S. Brandani, *Adsorption*, 2021, **27**, 353-368.
72. J.-Y. Wang, E. Mangano, S. Brandani and D. M. Ruthven, *Adsorption*, 2021, **27**, 295-318.
73. A. Gupta, T. Stait-Gardner and W. S. Price, *Adsorption*, 2021, **27**, 503-533.
74. A. Baniani, S. J. Berens, M. P. Rivera, R. P. Lively and S. Vasenkov, *Adsorption*, 2021, **27**, 485-501.
75. J. Kärger, M. Avramovska, D. Freude, J. Haase, S. Hwang and R. Valiullin, *Adsorption*, 2021, **27**, 453-484.
76. J. J. E. Maris, D. Fu, F. Meirer and B. M. Weckhuysen, *Adsorption*, 2021, **27**, 423-452.
77. N. S. Wilkins, A. Rajendran and S. Farooq, *Adsorption*, 2021, **27**, 397-422.
78. J. Caro, *Adsorption*, 2021, **27**, 283-293.
79. T. M. Tovar, J. Zhao, W. T. Nunn, H. F. Barton, G. W. Peterson, G. N. Parsons and M. D. LeVan, *Journal of the American Chemical Society*, 2016, **138**, 11449-11452.
80. O. Zybalyo, O. Shekhah, H. Wang, M. Tafipolsky, R. Schmid, D. Johannsmann and C. Wöll, *Physical Chemistry Chemical Physics*, 2010, **12**, 8092-8097.
81. B. Smit, *Chemical Reviews*, 2008, **108**, 4125-4184.
82. Z. Zhao, Z. Li and Y. S. Lin, *Industrial and Engineering Chemistry Research*, 2009, **48**, 10015-10020.
83. S. Brandani, E. Mangano, F. Brandani and P. Pullumbi, *Separation and Purification Technology*, 2020, **245**, 116862.
84. W. Zhou, C. Wöll and L. Heinke, *Materials*, 2015, **8**, 3767-3775.
85. S. Brandani and E. Mangano, *Adsorption*, 2020, **1**, 3-3.
86. J. Liu, Y. Wang, A. I. Benin, P. Jakubczak, R. R. Willis and M. D. LeVan, *Langmuir*, 2010, **26**, 14301-14307.
87. M. I. Hossain and T. G. Glover, *Industrial & Engineering Chemistry Research*, 2019, DOI: 10.1021/acs.iecr.9b00976.
88. Y. Wang and M. D. LeVan, *Industrial and Engineering Chemistry Research*, 2007, **46**, 2141-2154.
89. H. Jobic, *Physical Chemistry Chemical Physics*, 1999, **1**, 525-530.
90. H. Jobic and D. N. Theodorou, *Microporous and Mesoporous Materials*, 2007, **102**, 21-50.
91. H. Jobic, D. I. Kolokolov, A. G. Stepanov, M. M. Koza and J.

- Ollivier, *Journal of Physical Chemistry C*, 2015, **119**, 16115-16120.
92. F. Salles, H. Jobic, A. Ghoulfi, P. L. Llewellyn, C. Serre, S. Bourrelly, G. Férey and G. Maurin, *Angewandte Chemie - International Edition*, 2009, **48**, 8335-8339.
93. H. Jobic, *Physical Chemistry Chemical Physics*, 2016, **18**, 17190-17195.
94. F. Stallmach, S. Gröger, V. Künzel, J. Kärger, O. M. Yaghi, M. Hesse and U. Müller, *Angewandte Chemie International Edition*, 2006, **45**, 2123-2126.
95. M. Peksa, J. Lang and F. Stallmach, *Microporous and Mesoporous Materials*, 2015, **205**, 11-15.
96. U. Hong, J. Kärger, R. Kramer, H. Pfeifer, G. Seiffert, U. Müller, K. K. Unger, H. B. Lück and T. Ito, *Zeolites*, 1991, **11**, 816-821.
97. B.-T. L. Bleken, K. P. Lillerud, T. Splith, A.-K. Pusch and F. Stallmach, *Microporous and Mesoporous Materials*, 2013, **182**, 25-31.
98. A. C. Forse, S. A. Altobelli, S. Benders, M. S. Conradi and J. A. Reimer, *Journal of Physical Chemistry C*, 2018, **122**, 15344-15351.
99. A. C. Forse, M. I. Gonzalez, R. L. Siegelman, V. J. Witherspoon, S. Jawahery, R. Mercado, P. J. Milner, J. D. Martell, B. Smit, B. Blümich, J. R. Long and J. A. Reimer, *Journal of the American Chemical Society*, 2018, **140**, 1663-1673.
100. S. Hertel, M. Wehring, S. Amirjalayer, M. Gratz, J. Lincke, H. Krautscheid, R. Schmid and F. Stallmach, *Eur. Phys. J. Appl. Phys.*, 2011, **55**, 20702-20702.
101. R. Thoma, J. Kärger, N. de Sousa Amadeu, S. Nießing and C. Janiak, *Chemistry - A European Journal*, 2017, **23**, 13000-13005.
102. J. Li, S. Li, A. Zheng, X. Liu, N. Yu and F. Deng, *Journal of Physical Chemistry C*, 2017, **121**, 14261-14268.
103. D. I. Kolokolov, A. G. Maryasov, J. Ollivier, D. Freude, J. Haase, A. G. Stepanov and H. Jobic, *Journal of Physical Chemistry C*, 2017, **121**, 2844-2857.
104. K. Chakarova, I. Strauss, M. Mihaylov, N. Drenchev and K. Hadjiivanov, *Microporous and Mesoporous Materials*, 2019, **281**, 110-122.
105. C. Chmelik and J. Kärger, *Adsorption*, 2010, **16**, 515-523.
106. P. V. Kortunov, L. Heinke, M. Arnold, Y. Nedellec, D. J. Jones, J. Caro and J. Kärger, *Journal of the American Chemical Society*, 2007, **129**, 8041-8047.
107. S. Han, T. M. Hermans, P. E. Fuller, Y. Wei and B. A. Grzybowski, *Angewandte Chemie International Edition*, 2012, **51**, 2662-2666.
108. R. Wang, B. C. Bukowski, J. Duan, T. R. Sheridan, A. Atilgan, K. Zhang, R. Q. Snurr and J. T. Hupp, *Langmuir*, 2020, **36**.
109. D. Saha, Z. Bao, F. Jia and S. Deng, *Environmental Science and Technology*, 2010, **44**, 1820-1826.
110. B. C. Bukowski, F. J. Keil, P. I. Ravikovitch, G. Sastre, R. Q. Snurr and M.-O. Coppens, *Adsorption*, 2021, DOI: 10.1007/s10450-021-00314-y.
111. C. R. Groom, I. J. Bruno, M. P. Lightfoot and S. C. Ward, *Acta Crystallographica Section B*, 2016, **72**, 171-179.
112. Y. G. Chung, E. Haldoupis, B. J. Bucior, M. Haranczyk, S. Lee, H. Zhang, K. D. Vogiatzis, M. Milisavljevic, S. Ling, J. S. Camp, B. Slater, J. I. Siepmann, D. S. Sholl and R. Q. Snurr, *Journal of Chemical and Engineering Data*, 2019, **64**, 5985-5998.
113. S. Velioglu and S. Keskin, *Materials Advances*, 2020, **1**, 341-353.
114. C. E. Wilmer, M. Leaf, C. Y. Lee, O. K. Farha, B. G. Hauser, J. T. Hupp and R. Q. Snurr, *Nature Chemistry*, 2012, **4**, 83-89.
115. Y. J. Colón, D. A. Gómez-Gualdrón and R. Q. Snurr, *Crystal Growth & Design*, 2017, **17**, 5801-5810.
116. R. Anderson and D. A. Gómez-Gualdrón, *CrystEngComm*, 2019, **21**, 1653-1665.
117. P. G. Boyd and T. K. Woo, *CrystEngComm*, 2016, **18**, 3777-3792.
118. A. K. Rappe, C. J. Casewit, K. S. Colwell, W. A. Goddard and W. M. Skiff, *Journal of the American Chemical Society*, 1992, **114**, 10024-10035.
119. S. L. Mayo, B. D. Olafson and W. A. Goddard, *The Journal of Physical Chemistry*, 1990, **94**, 8897-8909.
120. D. C. Ford, D. Dubbeldam, R. Q. Snurr, V. Künzel, M. Wehring, F. Stallmach, J. Kärger and U. Müller, *The Journal of Physical Chemistry Letters*, 2012, **3**, 930-933.
121. L. Sarkisov, T. Düren and R. Q. Snurr, *Molecular Physics*, 2004, **102**, 211-221.
122. C. Serre, S. Bourrelly, A. Vimont, N. A. Ramsahye, G. Maurin, P. L. Llewellyn, M. Daturi, Y. Filinchuk, O. Leynaud, P. Barnes and G. Férey, *Advanced Materials*, 2007, **19**, 2246-2251.
123. J. Heinen and D. Dubbeldam, *WIREs Computational Molecular Science*, 2018, **8**, e1363.
124. L. Vanduyfhuys, S. Vandenbrande, T. Verstraelen, R. Schmid, M. Waroquier and V. Van Speybroeck, *Journal of Computational Chemistry*, 2015, **36**, 1015-1027.
125. L. Vanduyfhuys, S. Vandenbrande, J. Wieme, M. Waroquier, T. Verstraelen and V. Van Speybroeck, *Journal of Computational Chemistry*, 2018, **39**, 999-1011.
126. M. A. Addicoat, N. Vankova, I. F. Akter and T. Heine, *Journal of Chemical Theory and Computation*, 2014, **10**, 880-891.
127. D. E. Coupry, M. A. Addicoat and T. Heine, *Journal of Chemical Theory and Computation*, 2016, **12**, 5215-5225.
128. A. K. Rappe and W. A. Goddard, *The Journal of Physical Chemistry*, 1991, **95**, 3358-3363.
129. C. E. Wilmer, K. C. Kim and R. Q. Snurr, *The Journal of Physical Chemistry Letters*, 2012, **3**, 2506-2511.
130. E. S. Kadantsev, P. G. Boyd, T. D. Daff and T. K. Woo, *The Journal of Physical Chemistry Letters*, 2013, **4**, 3056-3061.
131. B. A. Wells, C. De Bruin-Dickason and A. L. Chaffee, *The Journal of Physical Chemistry C*, 2015, **119**, 456-466.
132. S. Kancharlapalli, A. Gopalan, M. Haranczyk and R. Q. Snurr, *Journal of Chemical Theory and Computation*, 2021, DOI: 10.1021/acs.jctc.0c01229.
133. V. V. Korolev, A. Mitrofanov, E. I. Marchenko, N. N. Eremin, V. Tkachenko and S. N. Kalmykov, *Chemistry of Materials*, 2020, **32**, 7822-7831.
134. A. Raza, A. Sturluson, C. M. Simon and X. Fern, *The Journal of Physical Chemistry C*, 2020, **124**, 19070-19082.
135. M. G. Martin and J. I. Siepmann, *The Journal of Physical Chemistry B*, 1998, **102**, 2569-2577.
136. B. Chen, J. J. Potoff and J. I. Siepmann, *The Journal of Physical Chemistry B*, 2001, **105**, 3093-3104.
137. C. D. Wick, M. G. Martin and J. I. Siepmann, *The Journal of Physical Chemistry B*, 2000, **104**, 8008-8016.
138. L. Zhang and J. I. Siepmann, *The Journal of Physical Chemistry B*, 2005, **109**, 2911-2919.
139. N. Sokkalingam, G. Kamath, M. Coscione and J. J. Potoff, *The Journal of Physical Chemistry B*, 2009, **113**, 10292-10297.
140. W. L. Jorgensen, J. D. Madura and C. J. Swenson, *Journal of the American Chemical Society*, 1984, **106**, 6638-6646.
141. V. Van Speybroeck, K. Hemelsoet, L. Joos, M. Waroquier, R. G. Bell and C. R. A. Catlow, *Chemical Society Reviews*, 2015, **44**, 7044-7111.

142. J. W. Harris, J. S. Bates, B. C. Bukowski, J. Greeley and R. Gounder, *ACS Catalysis*, 2020, **10**, 9476-9495.
143. B. J. Alder and T. E. Wainwright, *The Journal of Chemical Physics*, 1957, **27**, 1208-1209.
144. D. Frenkel and B. Smit, in *Understanding Molecular Simulation (Second Edition)*, eds. D. Frenkel and B. Smit, Academic Press, San Diego, 2002, DOI: <https://doi.org/10.1016/B978-012267351-1/50006-7>, pp. 63-107.
145. E. Vargas L and R. Q. Snurr, *Langmuir*, 2015, **31**, 10056-10065.
146. T. Savin and P. S. Doyle, *Physical Review E*, 2007, **76**, 021501.
147. E. J. Maginn, A. T. Bell and D. N. Theodorou, *The Journal of Physical Chemistry*, 1993, **97**, 4173-4181.
148. S. Velioglu and S. Keskin, *Journal of Materials Chemistry A*, 2019, **7**, 2301-2314.
149. A. F. Voter and J. D. Doll, *The Journal of Chemical Physics*, 1985, **82**, 80-92.
150. G. Mills, H. Jónsson and G. K. Schenter, *Surface Science*, 1995, **324**, 305-337.
151. G. Henkelman and H. Jónsson, *The Journal of Chemical Physics*, 1999, **111**, 7010-7022.
152. G. Henkelman and H. Jónsson, *The Journal of Chemical Physics*, 2000, **113**, 9978-9985.
153. G. Henkelman, B. P. Uberuaga and H. Jónsson, *The Journal of Chemical Physics*, 2000, **113**, 9901-9904.
154. A. Mace, S. Barthel and B. Smit, *Journal of Chemical Theory and Computation*, 2019, **15**, 2127-2141.
155. O. M. Braun and C. A. Sholl, *Physical Review B*, 1998, **58**, 14870-14879.
156. D. Dubbeldam, E. Beerdsen, S. Calero and B. Smit, *The Journal of Physical Chemistry B*, 2006, **110**, 3164-3172.
157. A. F. Voter, *Physical Review B*, 1986, **34**, 6819-6829.
158. A. B. Bortz, M. H. Kalos and J. L. Lebowitz, *Journal of Computational Physics*, 1975, **17**, 10-18.
159. R. J. Verploegh, Y. Wu, S. E. Boulfelfel and D. S. Sholl, *Journal of Physical Chemistry C*, 2018, **122**, 5627-5638.
160. A. Laio, A. Rodriguez-Forteza, F. L. Gervasio, M. Ceccarelli and M. Parrinello, *The Journal of Physical Chemistry B*, 2005, **109**, 6714-6721.
161. M. Iannuzzi, A. Laio and M. Parrinello, *Physical Review Letters*, 2003, **90**, 238302.
162. A. Laio and M. Parrinello, *Proceedings of the National Academy of Sciences*, 2002, **99**, 12562-12566.
163. C. Paolucci, I. Khurana, A. A. Parekh, S. Li, A. J. Shih, H. Li, J. R. Di Iorio, J. D. Albarracin-Caballero, A. Yezerets, J. T. Miller, W. N. Delgass, F. H. Ribeiro, W. F. Schneider and R. Gounder, *Science*, 2017, **357**, 898-903.
164. S. L. C. Moors, K. De Wispelaere, J. Van der Mynsbrugge, M. Waroquier and V. Van Speybroeck, *ACS Catalysis*, 2013, **3**, 2556-2567.
165. B. C. Bukowski, W. N. Delgass and J. Greeley, *The Journal of Physical Chemistry C*, 2021, **125**, 4519-4531.
166. G. R. Mcnamara and G. Zanetti, *Phys Rev Lett*, 1988, **61**, 2332-2335.
167. F. J. Higuera and J. Jimenez, *Europhys Lett*, 1989, **9**, 663-668.
168. S. Chen and G. D. Doolen, *Annu Rev Fluid Mech*, 1998, **30**, 329-364.
169. D. T. Thorne, *Lattice Boltzmann modeling: An introduction for geoscientists and engineers*, Springer, 2006.
170. J. Zhao, J. Yao, M. Zhang, L. Zhang, Y. Yang, H. Sun, S. An and A. Li, *Scientific Reports*, 2016, **6**, 32393.
171. J. L. Jiang, A. M. Plonka, A. I. Frenkel and D. Gersappe, *Journal of Physical Chemistry Letters*, 2018, **9**, 1092-1096.
172. C. Chmelik and J. Kärger, *Microporous and Mesoporous Materials*, 2016, **225**, 128-132.
173. E. Haldoupis, T. Watanabe, S. Nair and D. S. Sholl, *ChemPhysChem*, 2012, **13**, 3449-3452.
174. C. A. Downes and S. C. Marinescu, *ChemSusChem*, 2017, **10**, 4374-4392.
175. I. Stassen, N. Burtch, A. Talin, P. Falcaro, M. Allendorf and R. Ameloot, *Chemical Society Reviews*, 2017, **46**, 3185-3241.
176. V. Stavila, A. A. Talin and M. D. Allendorf, *Chemical Society Reviews*, 2014, **43**, 5994-6010.
177. M. D. Allendorf, A. Schwartzberg, V. Stavila and A. A. Talin, *Chemistry – A European Journal*, 2011, **17**, 11372-11388.
178. S. T. Meek, J. A. Greathouse and M. D. Allendorf, *Advanced Materials*, 2011, **23**, 249-267.
179. E. M. Johnson, S. Ilic and A. J. Morris, *ACS Central Science*, 2021, **7**, 445-453.
180. A. E. Baumann, D. A. Burns, B. Liu and V. S. Thoi, *Communications Chemistry*, 2019, **2**, 86.
181. Y. Xu, Q. Li, H. Xue and H. Pang, *Coordination Chemistry Reviews*, 2018, **376**, 292-318.
182. F. N. Al-Rowaili, A. Jamal, M. S. Ba Shammakh and A. Rana, *ACS Sustainable Chemistry & Engineering*, 2018, **6**, 15895-15914.
183. M. Ali, E. Pervaiz, T. Noor, O. Rabi, R. Zahra and M. Yang, *International Journal of Energy Research*, 2020, **n/a**.
184. B. D. McCarthy, A. M. Beiler, B. A. Johnson, T. Liseev, A. T. Castner and S. Ott, *Coordination chemistry reviews*, 2020, **406**, 213137.
185. B. A. Johnson, A. M. Beiler, B. D. McCarthy and S. Ott, *Journal of the American Chemical Society*, 2020, **142**, 11941-11956.
186. L. S. Xie, G. Skorupskii and M. Dincă, *Chemical Reviews*, 2020, **120**, 8536-8580.
187. N. A. SurrIDGE, C. S. Sosnoff, R. Schmehl, J. S. Facci and R. W. Murray, *The Journal of Physical Chemistry*, 1994, **98**, 917-923.
188. M. Lovrić and F. Scholz, *Journal of Solid State Electrochemistry*, 1997, **1**, 108-113.
189. P. J. Celis-Salazar, M. Cai, C. A. Cucinell, S. R. Ahrenholtz, C. C. Epley, P. M. Usov and A. J. Morris, *Journal of the American Chemical Society*, 2019, **141**, 11947-11953.
190. K. Timachova, H. Watanabe and N. P. Balsara, *Macromolecules*, 2015, **48**, 7882-7888.
191. W. Gorecki, M. Jeannin, E. Belorizky, C. Roux and M. Armand, *Journal of Physics: Condensed Matter*, 1995, **7**, 6823-6832.
192. K. Hayamizu, K. Sugimoto, E. Akiba, Y. Aihara, T. Bando and W. S. Price, *The Journal of Physical Chemistry B*, 2002, **106**, 547-554.
193. S. Bhattacharja, S. W. Smoot and D. H. Whitmore, *Solid State Ionics*, 1986, **18-19**, 306-314.
194. K. Timachova, I. Villaluenga, L. Cirrincione, M. Gobet, R. Bhattacharya, X. Jiang, J. Newman, L. A. Madsen, S. G. Greenbaum and N. P. Balsara, *The Journal of Physical Chemistry B*, 2018, **122**, 1537-1544.
195. S. J. Tambio, M. Deschamps, V. Sarou-Kanian, A. Etienne, T. Douillard, E. Maire and B. Lestriez, *Journal of Power Sources*, 2017, **362**, 315-322.
196. E. Kellenbach, M. Burgering and F. Kaspersen, *Organic Process Research & Development*, 1999, **3**, 141-144.
197. B. Corain, A. A. D'Archivio, L. Galantini, S. Lora, A. A. Isse and F. Maran, *Chemistry – A European Journal*, 2007, **13**, 2392-2401.

198. M. Cai, Q. Loague and A. J. Morris, *The Journal of Physical Chemistry Letters*, 2020, **11**, 702-709.
199. M. J. Powers, D. J. Salmon, R. W. Callahan and T. J. Meyer, *Journal of the American Chemical Society*, 1976, **98**, 6731-6733.
200. S. Goswami, I. Hod, J. D. Duan, C.-W. Kung, M. Rimoldi, C. D. Malliakas, R. H. Palmer, O. K. Farha and J. T. Hupp, *Journal of the American Chemical Society*, 2019, **141**, 17696-17702.
201. L. He, L. Yang, M. Dincă, R. Zhang and J. Li, *Angew. Chem.*, 2020, **132**, 9860-9866.
202. D. S. Sholl and R. P. Lively, *Nature*, 2016, **532**, 435-437.
203. *Materials for Separation Technologies: Energy and Emission Reduction Opportunities*, Oak Ridge National Laboratory.
204. Y. Wang and D. Zhao, *Crystal Growth and Design*, 2017, **17**, 2291-2308.
205. J. R. Li, R. J. Kuppler and H. C. Zhou, *Chemical Society Reviews*, 2009, **38**, 1477-1504.
206. J. R. Li, J. Sculley and H. C. Zhou, *Chemical Reviews*, 2012, **112**, 869-932.
207. E. Adatoz, A. K. Avci and S. Keskin, *Separation and Purification Technology*, 2015, **152**, 207-237.
208. M. S. Denny, J. C. Moreton, L. Benz and S. M. Cohen, *Nature Reviews Materials*, 2016, **1**, 16078.
209. D. M. Polyukhov, A. S. Poryvaev, S. A. Gromilov and M. V. Fedin, *Nano Letters*, 2019, **19**, 6506-6510.
210. X. Li, J. Wang, N. Bai, X. Zhang, X. Han, I. da Silva, C. G. Morris, S. Xu, D. M. Wilary, Y. Sun, Y. Cheng, C. A. Murray, C. C. Tang, M. D. Frogley, G. Cinque, T. Lowe, H. Zhang, A. J. Ramirez-Cuesta, K. M. Thomas, L. W. Bolton, S. Yang and M. Schröder, *Nature Communications*, 2020, **11**, 1-10.
211. L. Yang, S. Qian, X. Wang, X. Cui, B. Chen and H. Xing, *Chemical Society Reviews*, 2020, **49**, 5359-5406.
212. L. Yu, X. Dong, Q. Gong, S. R. Acharya, Y. Lin, H. Wang, Y. Han, T. Thonhauser and J. Li, *Journal of the American Chemical Society*, 2020, **142**, 6925-6929.
213. H. Wang, X. Dong, J. Lin, S. J. Teat, S. Jensen, J. Cure, E. V. Alexandrov, Q. Xia, K. Tan, Q. Wang, D. H. Olson, D. M. Proserpio, Y. J. Chabal, T. Thonhauser, J. Sun, Y. Han and J. Li, *Nature Communications*, 2018, **9**, 1-11.
214. B. L. Suh and J. Kim, *RSC Advances*, 2020, **10**, 22601-22605.
215. B. Slater, Z. Wang, S. Jiang, M. R. Hill and B. P. Ladewig, *Journal of the American Chemical Society*, 2017, **139**, 18322-18327.
216. M. N. Corella-Ochoa, J. B. Tapia, H. N. Rubin, V. Lillo, J. González-Cobos, J. L. Núñez-Rico, S. R. G. Balestra, N. Almora-Barrios, M. Lledós, A. Guèll-Bara, J. Cabezas-Giménez, E. C. Escudero-Adán, A. Vidal-Ferran, S. Calero, M. Reynolds, C. Martí-Gastaldó and J. R. Galán-Mascarós, *Journal of the American Chemical Society*, 2019, **141**, 14306-14316.
217. P. Z. Moghadam and T. Düren, *Journal of Physical Chemistry C*, 2012, **116**, 20874-20881.
218. D. Suttipat, S. Butcha, S. Assavapanumat, T. Maihom, B. Gupta, A. Perro, N. Sojic, A. Kuhn and C. Wattanakit, *ACS applied materials & interfaces*, 2020, **12**, 36548-36557.
219. Y. G. Chung, P. Bai, M. Haranczyk, K. T. Leperi, P. Li, H. Zhang, T. C. Wang, T. Duerinck, F. You, J. T. Hupp, O. K. Farha, J. I. Siepmann and R. Q. Snurr, *Chemistry of Materials*, 2017, **29**, 6315-6328.
220. S. Li, Y. G. Chung and R. Q. Snurr, *Langmuir*, 2016, **32**, 10368-10376.
221. H. Daglar and S. Keskin, *The Journal of Physical Chemistry C*, 2018, **122**, 17347-17357.
222. Y. Pramudya, S. Bonakala, D. Antypov, P. M. Bhatt, A. Shkurenko, M. Eddaoudi, M. J. Rosseinsky and M. S. Dyer, *Physical Chemistry Chemical Physics*, 2020, **22**, 23073-23082.
223. T. Watanabe and D. S. Sholl, *Langmuir*, 2012, **28**, 14114-14128.
224. A. Bavykina, N. Kolobov, I. S. Khan, J. A. Bau, A. Ramirez and J. Gascon, *Chemical Reviews*, 2020, **120**, 8468-8535.
225. J. Gascon, A. Corma, F. Kapteijn and F. X. Llabrés I Xamena, *ACS Catalysis*, 2014, **4**, 361-378.
226. B. A. Johnson, A. M. Beiler, B. D. McCarthy and S. Ott, *Journal of the American Chemical Society*, 2020, **142**, 11941-11956.
227. D. Yang, C. A. Gaggioli, D. Ray, M. Babucci, L. Gagliardi and B. C. Gates, *Journal of the American Chemical Society*, 2020, **142**, 8044-8056.
228. E. W. Thiele, *Industrial & Engineering Chemistry*, 1939, **31**, 916-920.
229. B. A. Johnson and S. Ott, *Chemical Science*, 2020, **11**, 7468-7478.
230. B. Tahmouresilerd, M. Moody, L. Agogo and A. F. Cozzolino, *Dalton Transactions*, 2019, **48**, 6445-6454.
231. A. Dhakshinamoorthy, M. Alvaro, Y. K. Hwang, Y. K. Seo, A. Corma and H. Garcia, *Dalton Transactions*, 2011, **40**, 10719-10724.
232. M. J. Katz, J. E. Mondloch, R. K. Totten, J. K. Park, S. T. Nguyen, O. K. Farha and J. T. Hupp, *Angewandte Chemie International Edition*, 2014, **53**, 497-501.
233. M. Agrawal, S. E. Bouffeffel, D. F. Sava Gallis, J. A. Greathouse and D. S. Sholl, *Journal of Physical Chemistry Letters*, 2019, **10**, 7823-7830.
234. G. W. Peterson, S.-Y. Moon, G. W. Wagner, M. G. Hall, J. B. DeCoste, J. T. Hupp and O. K. Farha, *Inorganic Chemistry*, 2015, **54**, 9684-9686.
235. X. Liu, K. O. Kirlikovali, Z. Chen, K. Ma, K. B. Idrees, R. Cao, X. Zhang, T. Islamoglu, Y. Liu and O. K. Farha, *Chemistry of Materials*, 2021, DOI: 10.1021/acs.chemmater.0c04675.
236. D. M. Kabtamu, Y. n. Wu and F. Li, *Journal of Hazardous Materials*, 2020, **397**, 122765-122765.
237. F. G. Cirujano, N. Martin and L. H. Wee, *Chemistry of Materials*, 2020, **32**, 10268-10295.
238. H. Zhang, J. Huo, J. Li, F. Li, C. Duan and H. Xi, *CrystEngComm*, 2018, **20**, 5754-5759.
239. Y. Qin, X. Han, Y. Li, A. Han, W. Liu, H. Xu and J. Liu, *ACS Catalysis*, 2020, **10**, 5973-5978.
240. Y. Li, Q. Gao, L. Zhang, Y. Zhou, Y. Zhong, Y. Ying, M. Zhang, C. Huang and Y. a. Wang, *Dalton Transactions*, 2018, **47**, 6394-6403.
241. C. T. Buru, M. C. Wasson and O. K. Farha, *ACS Applied Nano Materials*, 2020, **3**, 658-664.
242. M. Stuckart and K. Y. Monakhov, *Journal of Materials Chemistry A*, 2018, **6**, 17849-17853.
243. T. Guo, K. Mo, N. Zhang, L. Xiao, W. Liu and L. Wen, *Dalton Transactions*, 2021, DOI: 10.1039/D0DT03877F.
244. M. B. Majewski, A. J. Howarth, P. Li, M. R. Wasielewski, J. T. Hupp and O. K. Farha, *CrystEngComm*, 2017, **19**, 4082-4091.
245. H. Huang, K. Shen, F. Chen and Y. Li, *ACS Catalysis*, 2020, **10**, 6579-6586.
246. M. Zaarour, J. Cazemier and J. Ruiz-Martínez, *Catalysis Science & Technology*, 2020, **10**, 8140-8172.
247. J. Yu, C. Mu, B. Yan, X. Qin, C. Shen, H. Xue and H. Pang, *Materials Horizons*, 2017, **4**, 557-569.
248. Y. Chen, S. Han, X. Li, Z. Zhang and S. Ma, *Inorganic Chemistry*, 2014, **53**, 10006-10008.

Review Article

Chem Soc Rev

249. Q. Yue, Y. Lu, Z. Zhang, H. Tian, H. Wang, X. Li and S. Liu, *New Journal of Chemistry*, 2020, **44**, 16913-16920.
250. A. Zanon and F. Verpoort, *Coordination Chemistry Reviews*, 2017, **353**, 201-222.
251. Z. Guo, C. Xiao, R. V. Maligal-Ganesh, L. Zhou, T. W. Goh, X. Li, D. Tesfagaber, A. Thiel and W. Huang, *ACS Catalysis*, 2014, **4**, 1340-1348.
252. W. Zhang, W. Shi, W. Ji, H. Wu, Z. Gu, P. Wang, X. Li, P. Qin, J. Zhang, Y. Fan, T. Wu, Y. Fu, W. Zhang and F. Huo, *ACS Catalysis*, 2020, **10**, 5805-5813.
253. L. Hao, X. Li, M. J. Hurlock, X. Tu and Q. Zhang, *Chemical Communications*, 2018, **54**, 11817-11820.